2015-03-01

Simulations of Electron Trajectories in an Intense Laser Focus for Photon Scattering Experiments

Grayson J. Tarbox

Brigham Young University - Provo

www.manaraa.com

Simulations of Electron Trajectories in an Intense Laser Focus

for Photon Scattering Experiments

Grayson J. Tarbox

A thesis submitted to the faculty of
Brigham Young University
in partial fulfillment of the requirements for the degree of

Master of Science

Justin Peatross, Chair
Michael Ware
Jean-François Van Huele

Department of Physics and Astronomy

Brigham Young University

March 2015

ABSTRACT

Simulations of Electron Trajectories in an Intense Laser Focus
for Photon Scattering Experiments

Grayson J. Tarbox
Department of Physics and Astronomy, BYU
Master of Science

An experiment currently underway at BYU is designed to test whether the size of a free electron wave packet affects the character of scattered radiation. Using a semi-classical argument wherein the wave packet is treated as a diffuse charge distribution, one would expect strong suppression of radiation in the direction perpendicular to the propagating field as the wave packet grows in size to be comparable to the wavelength of the driving field. If one disallows the interaction of the wave packet with itself, as is the case when calculating the rate of emission using QED, then regardless of size, the electron wave packet radiates with the strength of a point-like emitter. In support of this experiment, we explore a variety of physical parameters that impact the rate of scattered photons. We employ a classical model to characterize the exposure of electrons to high-intensity laser light in a situation where the electrons are driven by strong ponderomotive gradients. Free electrons are modeled as being donated by low-density helium, which undergoes strong-field ionization early on in the pulse or during a pre-pulse. When exposed to relativistic intensities (i.e. intensities sufficient to cause a Lorentz drift at a significant fraction of c), free electrons experience a Lorentz drift that causes redshifting of the scattered 800 nm laser light. This redshift can be used as a key signature to discern light scattered from the more intense regions of the focus. We characterize the focal volume of initial positions leading to significant redshifting, given a peak intensity of 2×10^{18} W/cm^2, which is sufficient to cause a redshift in scattered light of approximately 100 nm. Under this scenario, the beam waist needs to be larger than several wavelengths for a pulse duration of 35 fs in order to ensure free electrons remain in the focus sufficiently long to experience intensities near the peak pulse intensity despite strong ponderomotive gradients. We compute the rate of redshifted scattered photons from an ensemble of electrons distributed throughout the focus and relate the result to the scattered-photon rate of a single electron. We also estimate to what extent the ionization process may produce unwanted light in the redshifted spectral region that may confound the measurement of light scattered from electrons experiencing intensities greater than 1.5×10^{18} W/cm^2.

ACKNOWLEDGMENTS

Contents

List of Figures

Chapter 1

Introduction

At intensities around and above $10^{18}\text{W}/\text{cm}^2$, free electrons inside a laser focus undergo relativistic motion for optical frequencies. The availability of high-intensity lasers during the past two decades has spurred a number of investigations into the behavior of electrons in such an environment. This includes ponderomotive acceleration, Lorentz drift, and plasma wakefield generation [1–7]. In addition, there have been efforts to observe Thomson scattering from relativistically excited plasmas [8–10]. Significant effort has also been made to develop theories and models that explain the dynamics of individual free-electrons in intense laser fields [11–15], as well as the associated scattered radiation [16–18]. In this thesis, we investigate how individual electrons radiate as they interact with a laser field.

1.1   Free Electrons in a Laser Focus

Classical electrodynamics teaches that accelerated charges emit electromagnetic radiation. In this paradigm, an electron is treated as a classical point particle. In quantum mechanics, however, the electron is represented by a wave function that forms a wave packet, which is extended in nature. As long as the wave function remains relatively small in comparison to the wavelength of light

1

www.manaraa.com
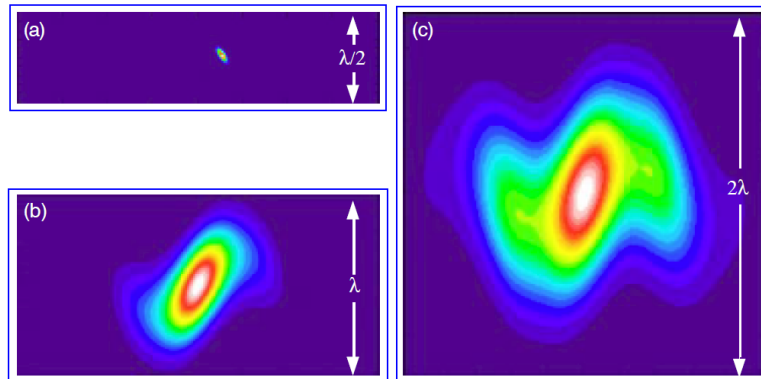
Figure 1.1 Depiction of a Volkov state solution for an electron in an intense laser field after (a) 0 cycles, (b) 50 cycles, and (c) 100 cycles as calculated in Ref. [15].

that may scatter from it, these two descriptions do not differ significantly from each other. High intensity lasers available today can easily achieve fields in excess of 10^{18} W/cm^2, where relativistic effects take place. In such intense fields, atoms such as helium quickly ionize, and the liberated electrons oscillate in the field at relativistic speeds, experiencing accelerations above 10^{22} m/s^2. An electron wave packet can quickly spread from an initially compact state to one that measures microns across or larger. Thus, in the presence of an intense laser field, an electron wave packet can easily spread to become comparable in size to the laser wavelength. Different parts of the same electron wave packet then oscillate out of phase. In such cases, it is natural to ask how the electron wave packet radiates. An example of such spreading is depicted in Fig. 1.1.

One might be tempted to treat the electron wave packet as a diffuse, classical extended charge distribution. From this perspective, the evolution of the wave packet is governed by quantum mechanics (in the limit of weak radiative feedback) while its photoemission is governed by classical electrodynamics. Under this (incorrect) viewpoint, different portions of the wave packet interfere, resulting in strong suppression of light scattered out the side of the focus. Conceptually, this viewpoint is difficult to maintain because it requires different portions of the same electron wave packet to perform work on other parts, as demonstrated in the next section.
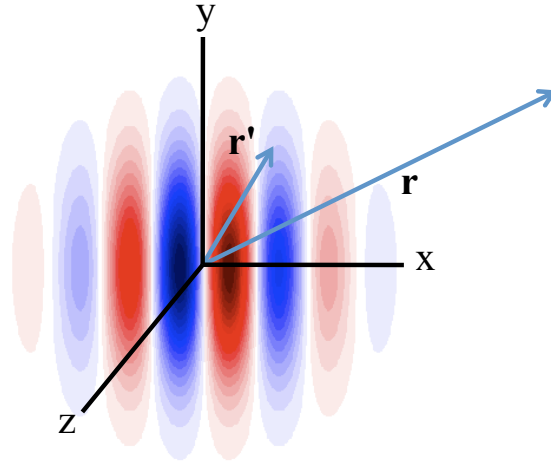
Figure 1.2 A Gaussian current distribution defined by Eq.(1.1). The direction of the current alternates with each stripe and is polarized in the z-direction. Internal waves propagate in the x-direction at *c* while the distribution remains centered at the origin.

1.2 Example: Oscillating Classical Current Distribution

Consider interference within the context of far-field radiation from classical current distributions in order to build better intuition for quantum radiation scattering [19]. We examine a classical current distribution designed to mimic a free quantum wave packet for a charged particle stimulated by a laser field. If such a wave packet is sufficiently diffuse to make quantum spreading slow and if an applied laser field avoids the relativistic regime such that we may neglect geometrical distortions to the shape, then we may contemplate a current distribution with the following form:

$$\mathbf{J}\left(\mathbf{r}',t\right) = \hat{z}J_0 e^{-r'^2/r_0^2} \sin\left(kx' - \omega t\right). \tag{1.1}$$

This scenario arises when a Gaussian charge distribution is stimulated by an external electric field polarized in the *z*-direction and traveling in the *x*-direction with frequency $\omega = ck$. This current distribution is depicted in Fig. 1.2.

When Eq. (1.1) is inserted into Jefimenko's equation [20] for the electric field, we obtain

$$
\begin{aligned}
\mathbf{E}(\mathbf{r},t) = \frac{J_0}{4\pi\varepsilon_0\omega} \int e^{-r'^2/r_0^2} &\left[(3(\hat{z}\cdot\hat{\mathbf{r}}_{ret})\hat{\mathbf{r}}_{ret} - \hat{z}) \left[\frac{\cos(kx'-\omega t + kr_{ret})}{r_{ret}^3} + \frac{k\sin(kx'-\omega t + kr_{ret})}{r_{ret}^2} \right] \right. \\
&\left. - ((\hat{z}\cdot\hat{\mathbf{r}}_{ret})\hat{\mathbf{r}}_{ret} - \hat{z}) \frac{k^2\cos(kx'-\omega t + kr_{ret})}{r_{ret}} \right] d^3r' + \frac{1}{4\pi\varepsilon_0}\int d^3r' \frac{\rho_{static}(\mathbf{r}')}{r_{ret}^2}\hat{\mathbf{r}}_{ret}
\end{aligned}
$$
$$(1.2)$$

Aside from the electrostatic term, this field is identical to the field arising from a distribution of oscillating dipoles. J_0/ω may be thought of as the peak medium polarization (in units of dipoles per volume).

Only the term involving $1/r_{ret}$ in Eq. (1.2) survives in the far-field limit. In this limit we make the approximation $r_{ret} \approx r$ except in the cosine argument where we write $r_{ret} \cong r - \mathbf{r}'\cdot\hat{r}$. Eq. (1.2) then reduces to

$$
\begin{aligned}
\mathbf{E}(\mathbf{r},t) &\cong -\frac{kJ_0}{4\pi\varepsilon_0 cr}((\hat{z}\cdot\hat{r})\hat{r}-\hat{z})\int e^{-r'^2/r_0^2}\cos\left(kx'-\omega t + kr - k\frac{x'x+y'y+z'z}{r}\right)d^3r' \\
&= -\hat{\theta}\frac{kJ_0\sin\theta}{4\pi\varepsilon_0 c}\mathrm{Re}\,\frac{e^{i(kr-\omega t)}}{r}\int_{-\infty}^{\infty}dx' e^{-\frac{x'^2}{r_0^2}}e^{-ik\left(\frac{x}{r}-1\right)x'}\int_{-\infty}^{\infty}dy' e^{-\frac{y'^2}{r_0^2}}e^{-ik\frac{y}{r}y'}\int_{-\infty}^{\infty}dz' e^{-\frac{z'^2}{r_0^2}}e^{-ik\frac{z}{r}z'}
\end{aligned}
$$
$$(1.3)$$

After performing the Gaussian integrals, the electric field simplifies to

$$
\mathbf{E}(\mathbf{r},t) \cong -\hat{\theta}J_0\frac{k\sqrt{\pi}r_0^3}{4\varepsilon_0 c}\sin\theta\frac{\cos(kr-\omega t)}{r}e^{-\frac{k^2r_0^2}{2}(1-\sin\theta\cos\phi)}
$$
$$(1.4)$$

with $x/r = \sin\theta\cos\phi$.

The average Poynting flux (directed along $\hat{r}$) is given by the expression

$$
\langle S\rangle_t = \varepsilon_0 c\left\langle |\mathbf{E}|^2\right\rangle_t = \frac{k^2\pi J_0^2 r_0^6}{32\varepsilon_0 c}\frac{\sin^2\theta e^{-k^2 r_0^2(1-\sin\theta\cos\phi)}}{r^2}.
$$
$$(1.5)$$

This expression is shown in Fig. 1.3 for various distribution sizes. As the size of the source current distribution grows, interferences cause the emitted radiation to be suppressed in every direction except along the *x*-axis, the direction of the traveling wave responsible for stimulating the current. This constructive interference in a preferred direction is commonly referred to as phase matching.

To compute the average power radiated into the far field, we insert Eq. (1.5) into $\langle P \rangle_t = r^2 \int\limits_0^{2\pi} d\phi \int\limits_0^{\pi} d\theta \sin\theta \langle S \rangle_t$ which after integration yields

$$\langle P \rangle_t = \frac{\pi^2 J_0^2 r_0^4}{16\varepsilon_0 c} \left[1 - e^{-2(kr_0)^2} - \frac{1 + e^{-2(kr_0)^2}}{(kr_0)^2} + \frac{1 - e^{-2(kr_0)^2}}{(kr_0)^4} \right]. \tag{1.6}$$

A graph showing the total radiated power is given in Fig. 1.4. As the size kr_0 of the (normalized) current distribution increases, the relative overall power drops off as the emission into directions other than the *x*-axis is suppressed.

Poynting's theorem guarantees that on average the radiated power precisely balances the power necessary to maintain the current, as described by

$$P = -\int \mathbf{E}(\mathbf{r},t) \cdot \mathbf{J}(\mathbf{r},t) \, d^3 r. \tag{1.7}$$

When we explicitly install Eqs. (1.1) and (1.2) in Eq. (1.7), we generate the following six-dimensional integral:

$$\langle P \rangle_t = \frac{J_0^2 k^2}{8\pi\varepsilon_0 c} \int d^3 r \, e^{-r^2/r_0^2} \int d^3 r' e^{-r'^2/r_0^2}$$
$$\times \left[\left(\frac{3(\hat{z}\cdot\hat{\mathbf{r}}_{ret})^2 - 1}{(kr_{ret})^3} - \frac{(\hat{z}\cdot\hat{\mathbf{r}}_{ret})^2 - 1}{kr_{ret}} \right) \sin(kr_{ret} - kr_{ret,x}) - \frac{3(\hat{z}\cdot\hat{\mathbf{r}}_{ret})^2 - 1}{(kr_{ret})^2} \cos(kr_{ret} - kr_{ret,x}) \right], \tag{1.8}$$

where we have used $\langle \sin(kx - \omega t)\cos(kx' - \omega t + kr_{ret}) \rangle_t = -\sin(kr_{ret} - kr_{ret,x})/2$ and $\langle \sin(kx - \omega t)\sin(kx' - \omega t + kr_{ret}) \rangle_t = \cos(kr_{ret} - kr_{ret,x})/2$ with $r_{ret,x} \equiv x - x'$. When we carry out this integration, the result agrees precisely with Eq. (1.6), as expected. It is interesting that the near-field terms play an important role in computing Eq. (1.8), whereas only the far-field portion is needed to compute Eq. (1.6). The near-field work actually accounts for the diminished radiated power.

To summarize, we analyzed radiation emitted by a Gaussian-shaped current distribution with propagating internal oscillations using the framework of classical electrodynamics. The overall radiated power, as well as the radiation's spatial distribution, depends strongly on the extent of the
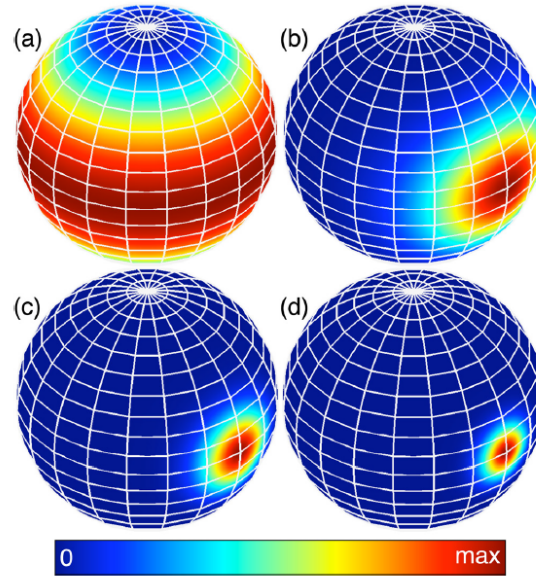
Figure 1.3 The far-field average Poynting flux for a Gaussian current distribution with distribution sizes (a) $kr_0 = 0$, (b) $kr_0 = 2\pi/3$, (c) $kr_0 = 4\pi/3$, and (d) $kr_0 = 2\pi$.

Gaussian distribution producing it. We demonstrated explicitly the connection between interference in the far field and the near-field work between different source components.

1.3 Quantum Electrodynamics and Pointlike Emission

The essential role of near-field work, particularly as it relates to far-field radiation, can provide insight into the behavior of a quantum system. A Gaussian current distribution is a classical analog that mimics the distribution of a Gaussian quantum wave packet for a charged particle in a laser field. A single-electron quantum wave packet with initial wave function $\psi(\mathbf{r},t)$ and charge e, however, must radiate quite differently than a classical charge density given by $\rho(\mathbf{r},t) = e|\psi(\mathbf{r},t)|^2$. At the most basic level, a classical charge density may perform work on itself via Coulomb self-repulsion. In contrast, accurate quantum mechanical results for the hydrogen atom are derived by excluding electron self-repulsion from the Hamiltonian. The removal of interferences in the scat-
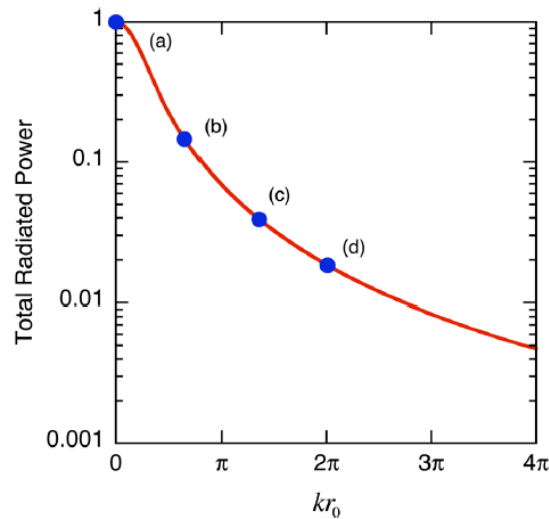
Figure 1.4 The total average power emitted from a Gaussian current distribution as a function of the distribution size with separations as given in Fig. 1.3. Power is expressed in units of the effective radiated dipole power for small kr_0.

tered radiation from a single quantum electron is as natural (and critical) as the omission of the classical Coulomb self-repulsion.

In a careful treatment of this problem using quantum electrodynamics Corson et al. demonstrated that, regardless of size, an electron wave packet radiates with the strength of a point-like emitter [21, 22]. In their analysis, they showed that the spatial size of a laser-driven electron wave packet does not affect the strength of the radiation, assuming the driving field is unidirectional. With coherent light sources, they also showed that energy-momentum conservation forbids interference in the scattered light to all orders of perturbation in QED. Then, working with the Furry picture of QED, interference was considered in the high-intensity limit. In this analysis, the matter fields were quantized using Volkov functions to treat the incident fields non-perturbatively. Within this high-intensity regime, they found a similar kinematic structure forbidding radiative interference.

The conclusion drawn from Corson's results is that, in contrast with classical electrodynamics where emissions from different regions of a charge current add coherently, the emission from

a quantum wave packet exhibits no interference. Quantum electrodynamics, with its subtleties, requires a different type of intuition; the spatial extent of a wave packet does not affect its radiation.

This second quantized description eliminates the possibility of the wave function performing work on itself. Under plausible experimental conditions, the difference in expected radiated intensity between the (incorrect) classical extended-charge picture and the correct QED treatment is approximately two orders of magnitude [18]. Such a difference should be testable, and so the group of Dr. Peatross and Dr. Ware have built an experiment to measure the intensity of light radiated out the side of a laser focus to distinguish between the two scenarios. My thesis work analyzes what might be expected in such a measurement. While I did not work on the apparatus myself, my work is important for the interpretation of the results.

1.4 Experimental Test of Laser Scattering from a Free Electron

1.4.1 Basic Design

An experiment is underway in our group at BYU, which is designed to measure photons emitted by free electrons out the side of a high-intensity laser focus, perpendicular to the direction of beam propagation. A titanium-sapphire laser system produces 75 mJ pulses of 800 nm light. The pulses enter the first of two large vacuum chambers where they are compressed temporally to 35 fs by diffraction gratings while preserving about 35 mJ of pulse energy. The compressed pulses are focused through a pinhole that separates the compression chamber from an interaction chamber.

The interaction chamber is evacuated to less than 10^{-8} torr and then backfilled with helium, which donates free electrons through ionization. An elliptical mirror images the focus at the pinhole into a much smaller spot with waist $w_0 \cong 5\mu$m. This gives an estimated peak intensity of

$$I = \frac{0.035\text{J}}{(35\text{fs})\frac{\pi}{2}(5\mu\text{m})^2} \cong 2 \times 10^{18}\frac{\text{W}}{\text{cm}^2} \tag{1.9}$$
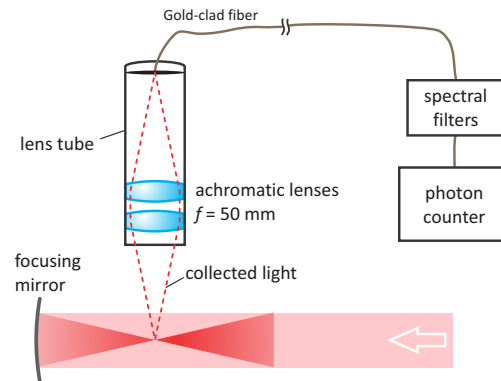
Figure 1.5 A schematic of the one-to-one imaging system used in the collection system for the electron radiation experiment.

With each laser pulse, the helium atoms in the laser focus become doubly ionized, and their electrons are accelerated in the intense laser field, causing them to radiate. A lens collects light emitted out the side of the laser focus. This light is collected using a one-to-one imaging system and is coupled into a gold-clad multi-mode fiber, which sends the collected photons to a spectrally filtered detector. The collection system is shown in Fig. 1.5 and subtends a solid angle of approximately 0.2 steradian.

1.4.2 Spectral and Temporal Filtering

An avalanche photodiode at the end of the fiber records single-photon events. An important feature of the experiment is the high intensity, which causes the free electrons in the most intense part of the focus to drift in the forward direction at a significant fraction of the speed of light. This effect, called the Lorentz drift because it originates from the $e\mathbf{v} \times \mathbf{B}$ force, causes the scattered photons, when viewed from the side of the focus, to be red shifted. This enables one to distinguish between the background laser light and photons of interest, which are scattered from electrons in the most intense part of the focus. The photons from the high-intensity interaction region possess both temporal and spectral characteristics that help differentiate them from background photons
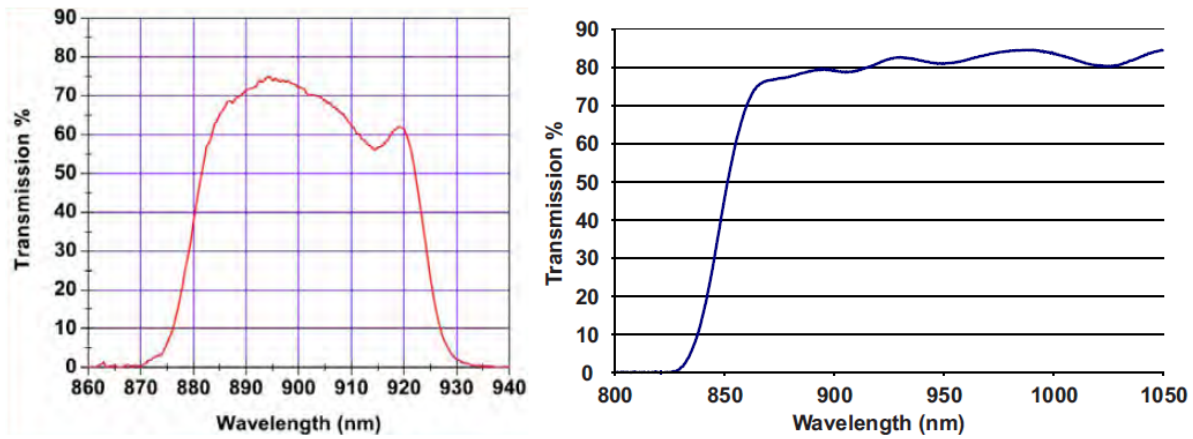
(a) Bandpass filter transmission specification

(b) High-pass filter transmission specification

Figure 1.6 Manufacturer specified transmission as a function of wavelength for (a) the bandpass filter, and (b) the high-pass filter [23].

(noise). This is crucial since the scattered events must be distinguished from the approximately 10^{17} photons in each laser pulse.

A spectral filtering system consisting of a bandpass and a long-pass filter is installed in front of the avalanche photodiode to block light near 800 nm while passing light in the 900 nm $\pm$ 25 nm range. Each filter allows approximately 70–80% of the 900 nm light to pass through while reducing the fundamental laser light by several orders of magnitude. The transmission profiles of the filters can be seen in Fig. 1.6.

The avalanche photodiode used to detect the collected photons, unfortunately, has a decreasing efficiency as the wavelength of light increases. Fig. 1.7 shows the specified detection efficiency, which should be taken into account as a factor when interpreting experimental data. The photons of interest also arrive at the detector within a certain time window, which allows us to distinguish them (with 0.1 ns instrument resolution) from other confounding noise sources such as light scattered from the chamber wall.
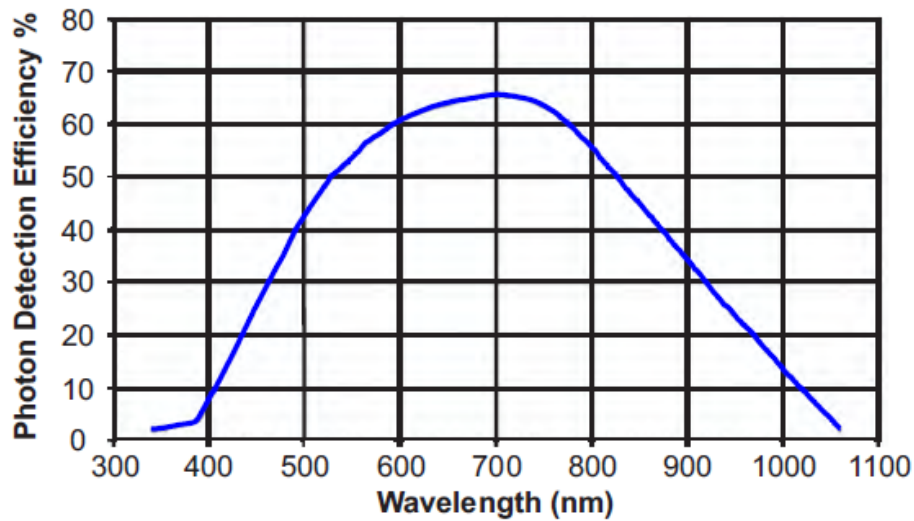
Figure 1.7 The manufacturer specified avalanche photodiode efficiency as a function of the incident light wavelength.

1.5   Simulations

I performed a series of numerical simulations to help determine an ideal set of parameters for the BYU experiment. An estimate of the intensity required to generate a redshift into the bandpass region was found to be $1.5 \times 10^{18} \mathrm{W/cm^2}$ per electron. We determined that the laser focus should have a waist greater than about 6 laser wavelengths in order to avoid overly strong ponderomotive gradients that tend to push electrons out of the focus prior to experiencing high intensities. The simulations show that in-band radiation output by electrons that experience 1.5×10^{18} W/cm^2 is several orders of magnitude greater than the radiation output from electrons that experience an intensity only just sufficient for ionization. This compensates for the fact that there are vastly more electrons experiencing low intensity that might emit photons (in band to the detector) during the ionization process.

Within the high intensity region of the focus, the average spectral intensity in the direction of a detector is approximately $1 \times 10^{-5} \frac{\mathrm{eV}}{\Omega \cdot \mathrm{nm}}$. The spectral window of interest is approximately 50 nm

wide, and the collection system subtends a solid angle of about 0.2 steradians. Using these values, the expected energy per electron in the focus is approximately 1×10^{-4} eV. Given the detector efficiency for single photon events is only 5%, it is expected that a large number of atoms are needed in order to achieve a detectable signal, requiring a backfill pressure of around 5×10^{-5} Torr.

Chapter 2 provides an overview of the model used to simulate electron trajectories in a laser focus. The equations of motion are outlined, including a vector representation for the laser fields. Calculations are performed that determine which intensity is required for the mildly relativistic redshift sought in our experiment. The effects of beam waist size on the time an electron spends inside the high intensity region of a focus are explored. The parameters for the beam waist and intensity are used to determine the portion of the focus where start positions for an electron generate the desired redshift in emitted radiation. An examination of how the signal scales with the number of electrons is also performed. A simple model for helium ionization is used to determine the correlation of trajectories for the pair of electrons ionized from the same helium atom over the timescales in the experiment. A calculation is also performed to estimate the radiation emitted during the ionization process.

Chapter 3 determines the average radiation spectrum for an electron in the ionized region for comparison with an electron in a continuous plane-wave field. An estimate of the photon count rate in the experiment is determined as a function of the intensity of the incident laser pulse. A summary of the results is provided, along with an outlook of the feasibility of the electron radiation experiment.

Chapter 2

Electron Simulation Model

2.1 Electron Trajectories in an Intense Laser Focus

Using quantized models to simulate electron dynamics at relativistic intensities is a numerically in-
tensive endeavor [24, 25]. To make the calculations more manageable, Chowdhury et al. examined
the behavior of an electron wave packet ionizing in ultra high intensity laser fields using a hybrid
quantum/classical model [16]. First, they used a tunneling-ionization rate model to promote an
increasing fraction of the electron probability into the continuum. Once in the continuum, each
tiny portion of the wave packet was propagated as a classical point-like trajectory. Many point-like
elements taken together represented the free electron wave, and these different elements spread out
under the influence of the strong laser field. This approach is quite reasonable since the influence
of quantum spreading is tiny in comparison to the extreme forces of the laser field.

Taking the approach used by Chowdury et al. as inspiration for our model, we decided to
model the electron more crudely as a single classical point-like trajectory in the laser focus. In
our case, we seek only order-of-magnitude accuracy and can afford to model electron dynamics
and emission based on classical point-like electrons. In addition, this approach is consistent with

the strength of emission based on QED, which is one of the two viewpoints to be distinguished by the experiment at BYU. A much lower scattering rate (i.e. two orders of magnitude) would align with the (incorrect) first-quantized perspective where scattering in the direction perpendicular to the propagating laser field is strongly suppressed, owing to interference between different portions of the large wave packet.

We use classical electrodynamics in the interaction of the laser field with the electron, allowing for simulations to be performed conveniently on a desktop computer. The laboratory-frame acceleration of an electron in the presence of electric and magnetic fields (in MKS units) is given by the expression [20]

$$\mathbf{a} = \frac{d^2\mathbf{r}}{dt^2} = -\frac{e}{\gamma m}[\mathbf{E}_L + \mathbf{v} \times \mathbf{B}_L - \frac{\mathbf{v}(\mathbf{v} \cdot \mathbf{E}_L)}{c^2}]. \tag{2.1}$$

where e, m, and $\mathbf{v}$ are the charge, mass, and velocity of the electron, $\gamma = 1/\sqrt{1 - v^2/c^2}$ is the standard relativistic factor, and $\mathbf{E}_L$ and $\mathbf{B}_L$ are the electric and magnetic fields of the laser.

For the purposes of programming this equation, it is convenient to use a set of scaled units. Beginning with the time and position variables, we let

$$t' \equiv \nu t, \quad \mathbf{r}' \equiv \mathbf{r}/\lambda \tag{2.2}$$

where ν is the laser frequency, and λ is the laser wavelength in MKS units. The velocity in this system works out to be

$$\mathbf{v} = \frac{d\mathbf{r}}{dt} = \lambda \nu \frac{d\mathbf{r}'}{dt'} = c\mathbf{v}' \Rightarrow \mathbf{v}' = \frac{\mathbf{v}}{c}, \tag{2.3}$$

and the corresponding acceleration

$$\mathbf{a} = \nu c \frac{d\mathbf{v}'}{dt'} = \nu c \mathbf{a}' \Rightarrow \mathbf{a}' = \frac{\mathbf{a}}{\nu c}. \tag{2.4}$$

When the electric and magnetic fields are scaled according to

$$\mathbf{E}'_L = \frac{e\lambda}{mc^2}\mathbf{E}_L \quad \text{and} \quad \mathbf{B}'_L = \frac{e\lambda}{mc}\mathbf{B}_L \tag{2.5}$$

where *e* is the magnitude of the charge of an electron, and *m* is the mass of an electron in MKS units, Eq. (2.1) simplifies to

$$\mathbf{a}' = -\sqrt{1 - \mathbf{v}'^2}\left[\mathbf{E}'_L + \mathbf{v}' \times \mathbf{B}'_L - \mathbf{v}'(\mathbf{v}' \cdot \mathbf{E}'_L)\right]. \tag{2.6}$$

An adequate single-frequency representation for the vector fields in an intense laser focus can be found in work by Salamin [1], which is summarized in Appendix A. For the purposes of this analysis, a moving time envelope with wavefront curvature was appended *ad hoc* to Salamin's result rather than using the more correct method of superposing a range of single frequency solutions. These vector fields are the fields E_L and B_L that are substituted into Eq. (2.5) in order to determine the scaled electric and magnetic fields in Eq. (2.6). This equation can be solved to determine the electron's path in the laser field using standard Runge-Kutta methods. We employ the built in ode45 solver in MATLAB®. An initial state vector comprising the electron's initial position and velocity, in addition to the start and stop times of the simulation, are provided to the ODE solver along with a subroutine containing Eq. 2.6. With these tools in place, we can examine the impact of laser parameters on electron trajectories as well as proceed to determine the expected radiation scattered from such electrons.

2.2 Electron Radiation Spectrum Calculation

The trajectories calculated using Eq. (2.6) can be used to determine the fields radiated by a classical electron [20]:

$$\mathbf{E}_e = -\frac{e}{4\pi\varepsilon_0}\frac{r_{ret}}{(\mathbf{r}_{ret} \cdot \mathbf{u})^3}\left[(c^2 - v^2)\mathbf{u} + \mathbf{r}_r et \times (\mathbf{u} \times \mathbf{a})\right] \tag{2.7}$$

$$\mathbf{B}_e = \frac{1}{c}\hat{\mathbf{r}}_{ret} \times \mathbf{E}_e. \tag{2.8}$$

Here $\mathbf{u} \equiv c\hat{\mathbf{r}}_{ret} - \mathbf{v}$ and $\mathbf{r}_{ret} \equiv \mathbf{r} - \mathbf{w}(t_r)$, where $\mathbf{w}$ is the position of the electron and $t_r = r_{ret}/c$ is the retarded time. The self-force of the electron due to this radiated field is neglected in Eq. (2.1);
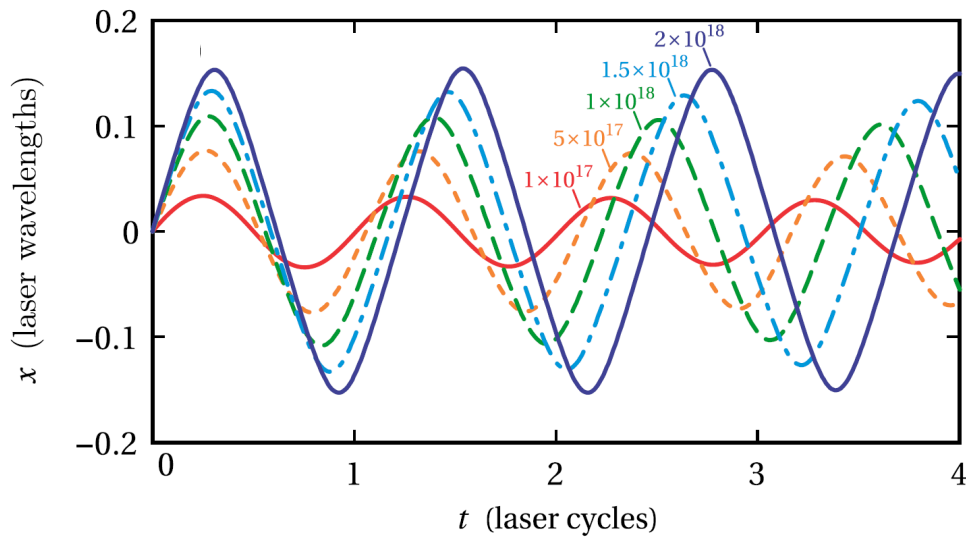
Figure 2.1 Oscillations of an electron near the peak of a plane-wave pulse with a Gaussian temporal window (FWHM) 35fs and $\lambda_L = 800$ nm. The phases of oscillation associated with the various peak intensities are shifted to align at $t = 0$ for easier comparison.

for optical driving fields, the radiation reaction force is approximately seven orders of magnitude below the force of the laser field. The spectrum of the scattered light, in a given location and with a given polarization direction, can be calculated by performing a Fourier transform on these fields.

For comparison with light scattered from a focused laser, we first show the results of simulations of light scattered by an unfocused plane-wave pulse propagating in the z direction having a Gaussian temporal envelope with duration 35 fs (FWHM). Figure 2.1 shows several transverse oscillations of a free electron as it interacts with such a plane-wave pulse near its peak for a variety of intensities. Note that the period of oscillations decreases as the Lorentz force causes the electron to drift with the propagating laser field at a significant fraction of c. Since the moving electron oscillates at a slower rate than the incident laser pulse, scattered light is red-shifted compared to the incident laser light. This effect becomes more pronounced as the laser intensity increases into the relativistic regime; as the drift velocity becomes an increasingly significant fraction of c, the amount of redshift in the scattered radiation increases. The trajectory of an electron interacting
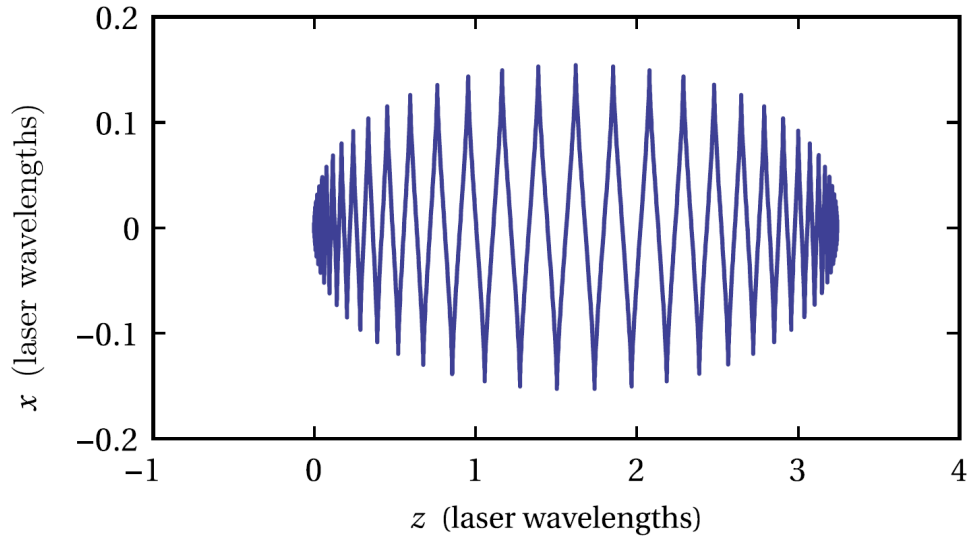
Figure 2.2 Trajectory of an electron experiencing a pulse with peak intensity $I_0 = 2 \times 10^{18} \text{W/cm}^2$.

with a laser pulse of peak intensity 2×10^{18} W/cm^2 over the course of a laser cycle can be seen in Fig. 2.2. During the course of the pulse, the electron drifts forward approximately three laser wavelengths in the direction of pulse propagation, and undergoes nonlinear motion (as noted by the trajectory no longer having a smooth, sinuous shape) before coming to rest again. The far-field intensity spectrum computed using Eqs. (2.7) – (2.8) for different peak intensities can be seen in Fig. 2.3. These spectra are calculated assuming a detector located in the direction perpendicular to both the pulse-propagation direction and the direction of the linear polarization. As seen in the figure, the spectrum undergoes an increasing amount of redshift and stronger emission as the laser pulse intensity increases. At the lowest intensity examined, $I_0 = 1 \times 10^{17}$ W/cm^2, the spectrum mostly resembles the spectrum of the incident pulse, being only slightly shifted from the spectral center of 800 nm. The ideal intensity for this experiment appears to be $I_0 = 1.5 \times 10^{18} \text{W/cm}^2$. This spectrum has the optimal amount of redshift for the experiment, keying in on the bandpass window of 875–925 nm.
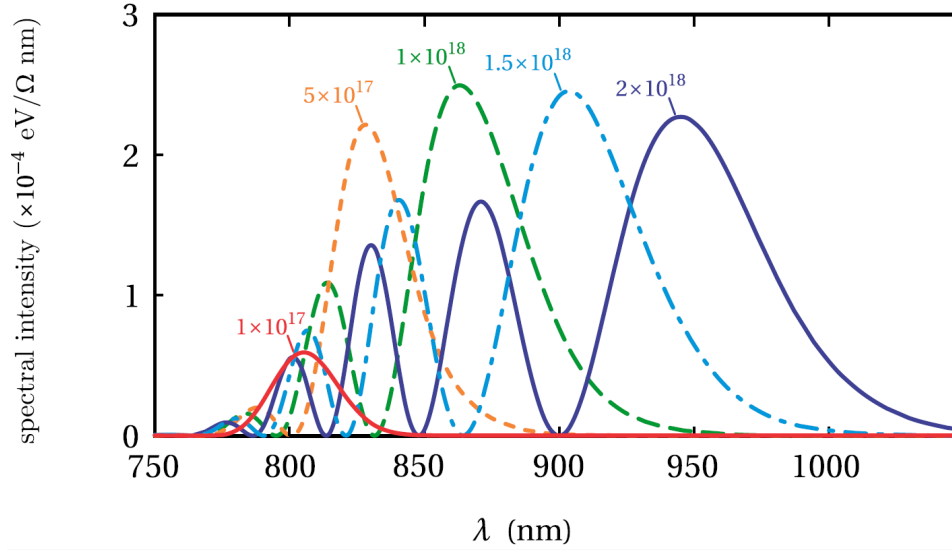
Figure 2.3 Far-field radiation spectrum in the direction perpendicular to both pulse propagation and the linear polarization generated by a free electron experiencing the various plane-wave pulses used in Fig. 2.1.

2.3   Determination of Minimum Beam Waist Size

Given finite laser pulse energy, we need a tight focus to achieve the desired relativistic intensities. Electrons in such a tight laser focus experience strong ponderomotive forces that tend to push them out the side of the focus, perhaps even before experiencing the maximum pulse intensity. The ponderomotive force is a nonlinear force experienced by charged particles in an inhomogeneous oscillating electromagnetic field, such as a laser field. The mechanism of the ponderomotive force can be thought of by considering the motion of the electron over the course of a laser cycle. In the case of a homogenous field (i.e. a plane wave field), the electron returns to its initial position in the *x* dimension after one laser cycle as shown in Figs. 2.1 and 2.2. When in an inhomogeneous field, such as a focused laser field, the force exerted on the electron during the half-cycle spent in the region with higher field amplitude points towards the region with lower amplitude. The force exerted on the electron during the half-cycle spent in the region with lower field amplitude points toward the region with higher amplitude, but is weaker. Over a full laser cycle, the net force

thus drives the electron toward regions with lower field amplitudes. Since it is proportional to the gradient of the magnitude squared of the electric field $|E|^2$, the more rapidly E varies spatially, as when a laser beam focuses tightly, the stronger the force pushing charged particles outside the focus. In addition, as a focus becomes smaller, electrons inside the high intensity region have a smaller distance to travel before escaping that region. Thus, it is important to characterize how tight the laser focus can be while still allowing the electrons sufficient time to experience the high intensity region.

For this simulation, we use a realistic representation of focused vector fields found in Appendix A. The peak intensity was fixed at $I_0 = 2 \times 10^{18}$ W/cm^2 with the same pulse duration used previously, 35 fs FWHM. With these parameters, the laser focus experiences about 10 laser cycles with an intensity above 1.5×10^{18} W/cm^2. These parameters, in fact, match those accessible in our laboratory with available equipment.

We consider first a laser focus with an extremely small beam waist $w_0 = \lambda_L$. With such a small focus, the ponderomotive gradient is very strong, causing electrons to leave the focus rapidly prior to experiencing the peak intensity of the pulse. Figure 2.4 depicts the trajectories of twenty different electrons positioned randomly within the most intense region of this laser focus. These electrons leave the focus rapidly before the pulse peak arrives, typically experiencing a maximum intensity a factor of 5 below the 2×10^{18} W/cm^2 peak. This laser focus is thus clearly too small for the proposed experiment since most electrons will never experience the intensity required to generate the desired redshift in the scattered radiation. Since it would be ideal to maximize the time spent within the high intensity region of the laser focus, this raises the question of what is the minimum focal size that is adequate for the experiment. It is also important to determine not just the size of the high-intensity region within a laser focus (as derived in Appendix B), but more specifically the volume of the region wherein the initial location of the electron gives rise to a trajectory that does not leave the focus prior to experiencing relativistic intensities.
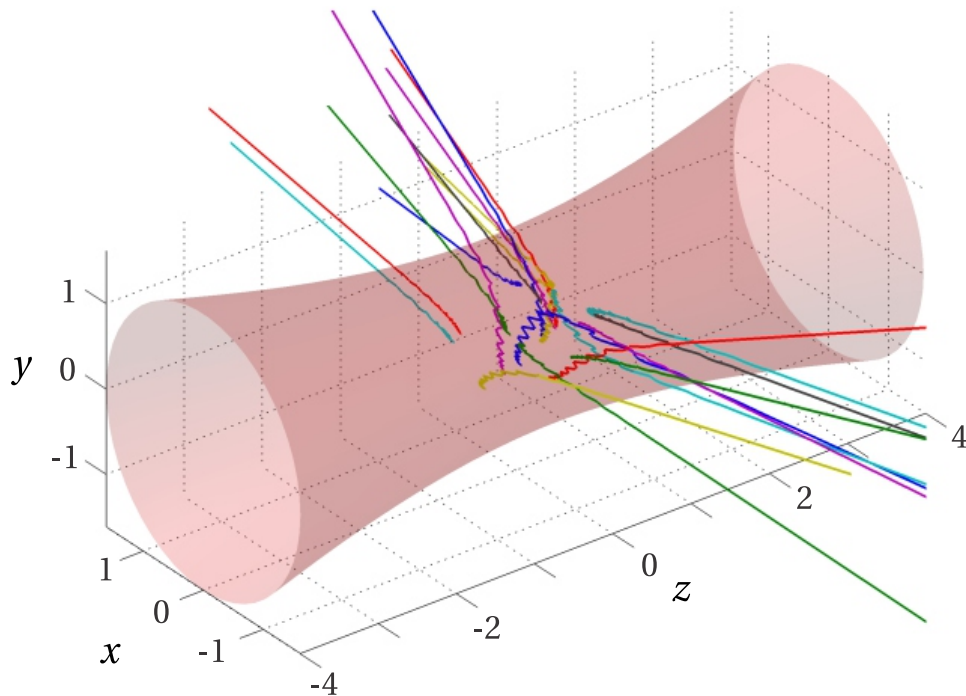
Figure 2.4 Simulated trajectories for 20 electrons starting within a laser pulse focused with a waist $w_0 = \lambda_L$. The laser pulse has a peak intensity of 2×10^{18} W/cm^2 and a duration of 35 fs FWHM. The electron initial positions are randomly distributed within the volume where the intensity is greater than 1×10^{18} W/cm^2. Due to strong ponderomotive forces, most are rapidly forced out of the focus prior to experiencing the pulse peak intensity.

In order to characterize the region wherein an electron's initial position gives rise to a trajectory that experiences relativistic intensities for a suitable duration, we ran a simulation in which electrons were released from various initial positions inside the focus. We computed their trajectories under the influence of the laser field, and monitored the intensity experienced by the electrons in order to determine how long they experience intensities above 1.5×10^{18} W/cm^2. The results of these simulations are shown in Fig. 2.5, indicating the average length of time that a free electron experiences at least 1.5×10^{18} W/cm^2 as a function of the beam waist w_0 while varying the initial position x_0, y_0, and z_0. In generating these plots, the electron was released from rest at its initial position when the laser field first exceeded the threshold for second ionization for helium, which is $I = 8.7 \times 10^{15}$ W/cm^2. The phase of the carrier-envelope can significantly affect the time spent within the high intensity region, so these simulations are also averaged over the carrier-envelope phase to account for this effect, which smooths out the resulting plots.

Figure 2.5 (a) depicts the duration of exposure to high intensity ($\geq 1.5 \times 10^{18}$ W/cm^2) for an electron that originates along the line $y_0 = 0$, $z_0 = 0$ for various values of x_0. Similarly, Fig. 2.5 (b) plots the duration of exposure to high intensity for an electron that originates along the line $x_0 = 0$, $z_0 = 0$ for various values of y_0. The laser pulse in the simulation is linearly polarized in the *x*-dimension. As the beam waist becomes large, an electron that begins near the center of the focus may experience the maximum 10 cycles of high intensity. However, if the beam waist narrows to less than $3\,\lambda_L$, the variety of positions that experience the requisite high intensity for any amount of time becomes extremely small. In this case, the tightly focused laser pulse produces ponderomotive gradients that pushes the electron outside the central portion of the focus before the highest intensity portion of the pulse arrives. Clearly, such a tight focus is undesirable for the proposed experiment. By increasing the size of the beam waist to $w_0 \approx 6\,\lambda_L$, there is a much greater variety of starting positions that experienced high intensities, and for an appreciable fraction of the maximum 10 laser cycles. More importantly, such a waist parameter is achievable with the laser
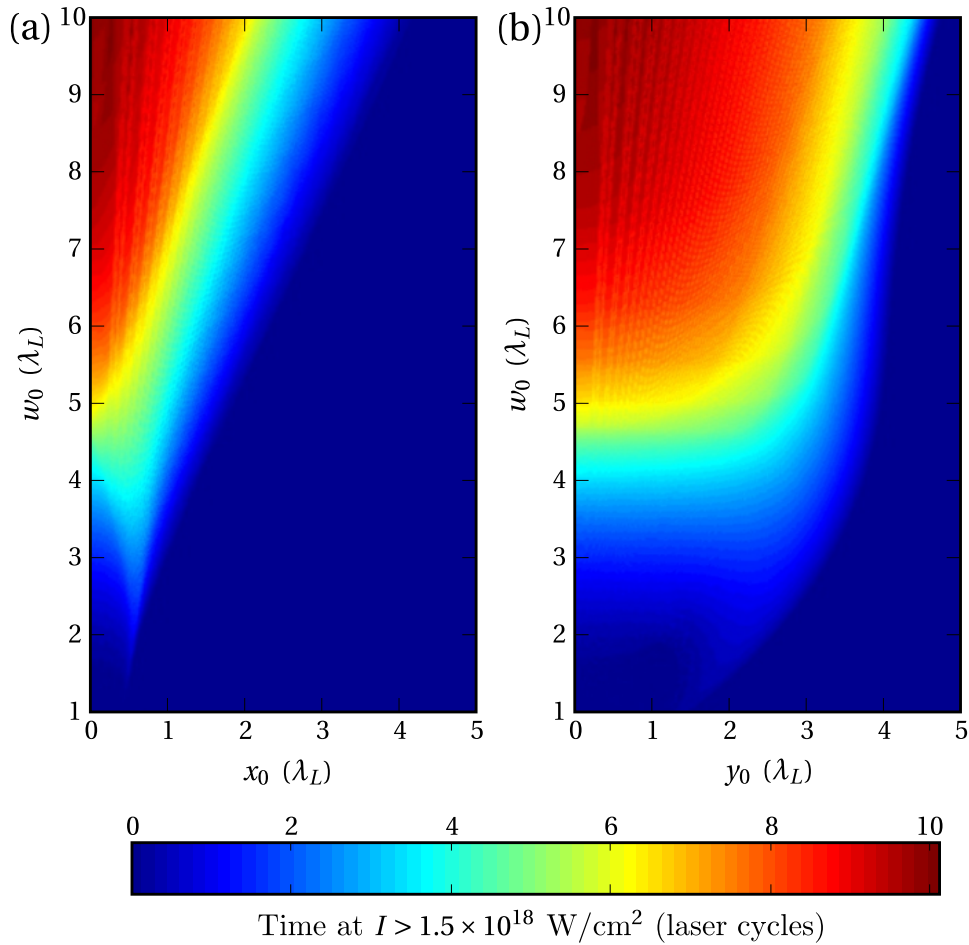
Figure 2.5 Time an electron experiences intensities $\geq 1.5 \times 10^{18}$ W/cm^2 as a function of the beam waist w_0 and the initial position (x_0, y_0, z_0). The electron was released from rest when the intensity first exceeded the second ionization threshold for helium. The peak intensity of the pulse was held at 2×10^{18} W/cm^2 with a duration of 35 fs FWHM. In (a) the initial position was $y_0 = 0$, $z_0 = 0$, while x_0 was varied. In (b) the initial postion was $x_0 = 0$, $z_0 = 0$, while y_0 was varied.
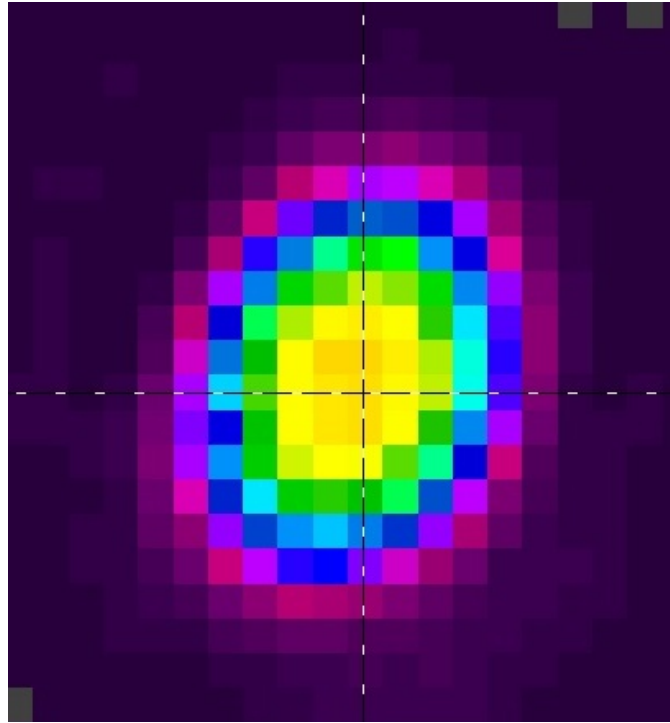
Figure 2.6 This is an image captured using a CCD camera of the focused laser beam in the electron radiation experiment taken at the pinhole. Pixels are square and 9.8μm $\times$ 9.8μm.

facility at BYU. To expose electrons to the desired high intensity for significantly longer times would require either a wider focus, or a special ponderomotive trapping scheme such as the one developed by Chaloupka et al. [26].

For the BYU experiment, the beam waist is about 5 μm, or approximately 6 laser wavelengths. A magnified image captured of the laser focus is shown in Fig. 2.6. The demagnification to the subsequent final focus is approximately a factor of 9, suggesting a beam waist of approximately 5 μm.

2.4   Effective Size of High-Intensity Region

To answer the question regarding the effective size of the high intensity focus, simulations were performed where electrons started from a variety of initial positions. Their trajectories were cal-

culated using the procedure outlined in Sec. 2.1. These electrons were then tracked to determine the intensities experienced along their individual trajectories. The results of these simulations are depicted in Fig. 2.7, showing both horizontal and vertical cross sections of the volume wherein the initial position enabled an electron to experience an intensity above 1.5×10^{18} W/cm^2. The coloring indicates the length of time an average electron experiences above that intensity, in units of laser cycles. For comparison, the laser intensity reaches an intensity greater than 1.5×10^{18} W/cm^2 within a radius of $\sqrt{x^2 + y^2} = 0.38\ w_0$, and within a longitudinal range of $|z| < 82\ \lambda_L$, which is a volume approximately six times the effective volume depicted in Fig. 2.7. Since electrons drift in the forward direction, note that initial positions located before the focus have an advantage. Also, since the linear polarization is in the *x*-dimension, initial positions that are offset from the axis in the *y*-dimension are preferable to positions that are offset from the axis in the *x*-dimension, noted by the thicker profile in the *y*-dimension.

2.5 Signal Scaling with Number of Electrons

While it would be conceptually ideal for the electron scattering experiment to have only one electron in the focus at a time, their location and number in the focus at any given time cannot be completely controlled. Moreover, efficiencies in the detector setup dictate that there needs to be many electrons in the focus to obtain a detectable signal for any practical experiment. It is important to understand how emissions from neighboring electrons interact. In particular, it is important to describe how the scattered radiation signal scales with the number of electrons and the density of helium atoms inside the laser focus.

The trajectories of the two electrons released from the same helium atom are initially correlated, so the pair radiates coherently, thus increasing the signal by a factor of two compared to the radiation from two separate and uncorrelated electrons. However, as will be discussed in Sec. 2.6,
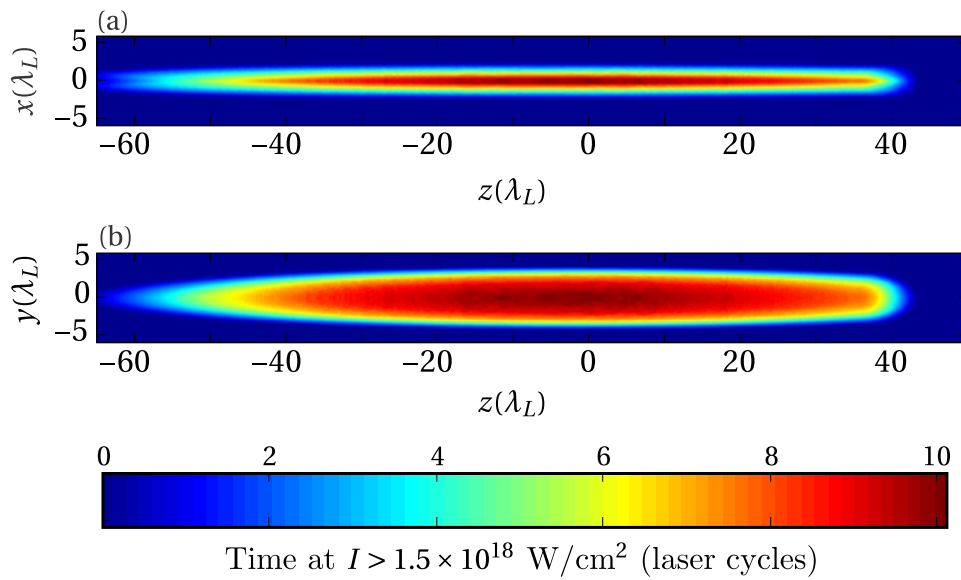
Figure 2.7 Two-dimensional slices in the (a) $x - z$ and (b) $y - z$ planes depicting the time an average electron experiences intensities greater than 1.5×10^{18} W/cm^2 plotted versus its initial position. Note that the positions offset from the axis in the y-dimension are preferable to positions offset in the x-dimension due to the linear polarization of the laser field in the x-dimension. Also, note that positions located before the focus are preferable since electrons drift in the upstream direction. The pulse parameters chosen for the simulations were $I_0 = 2 \times 10^{18}$ W/cm^2, $w_0 = 6\lambda_L$, $\lambda_L = 800$ nm, and $\tau_L = 35$ fs FWHM.

a pre-pulse can be employed in the experiment to pre-ionize the helium atoms prior to the arrival of the primary high intensity laser pulse. This allows some spreading and separation of the electrons to occur, limiting the coherence effect. In this case, the enhancement of the signal due to coherence effects should be negligible.

For electrons from separate atoms, the emission directed perpendicular to the direction of laser pulse propagation is incoherent if the electrons are distributed randomly throughout the focus, as demonstrated in Appendix C. Although there is a coherent buildup of emission in the forward direction, phase matching in the perpendicular direction is sufficiently poor to avoid coherence effects (except between electron pairs released from the same atom as discussed in the previous paragraph). In other words, the phases of emission from the various electrons may be treated as random since they are randomly located throughout the focus. In this case, the emission *intensities* for the individual electrons released from different atoms sum, on average, giving an expected total signal.

In order to confirm this intensity addition rule for the perpendicular direction, a simulation was performed to compute the emission from many electron pairs released from atoms positioned randomly throughout the focus. As anticipated, it was found that the overall emission fluctuates around an intensity equal to the single-atom intensity scaled by the number of atoms in the ensemble. Thus, for the purposes of interpreting experimental results, it is straightforward to connect the emission behavior of an ensemble including many free electrons to the single-electron emission behavior desired. However, it is crucial during the experiment that the density of helium backfilled into the interaction chamber be sufficiently low in order to avoid cooperative effects [27]. This mandates the electron spacing be greater than half a wavelength, limiting the donor-atom pressure to below 10^{-4} Torr.

2.6 Ionization and Spreading

Although hydrogen possesses a single electron in its monatomic state, it is found naturally in a diatomic state, and is highly reactive in its monatomic state. Helium, on the other hand, is inert and has just two electrons, making it the best donor atom available. In addition, the electrons in helium are liberated at higher intensities ($\approx 10^{16} \frac{W}{cm^2}$) than the first two electrons of any other potential donor atom or molecule.

The electrons in the scattering experiment are initially bound to a helium atom before quickly ionizing in the strong electromagnetic fields of a high intensity laser pulse. For our purposes, we use a strong-field ionization approximation to determine the intensities necessary to ionize helium [28, 29]. We model the two electrons by abruptly releasing the first one when an intensity of $1.3 \times 10^{15} W/cm^2$ is reached and releasing the second when an intensity of $8.7 \times 10^{15} W/cm^2$ is reached. We ignore the motion of the parent ion and focus attention on the two liberated electrons. An explanation of these intensities as well as a calculation of the volume inside the laser focus that experiences those intensities can be found in Appendix B. Figure 2.8 depicts the focal regions where first and second ionization of helium takes place along with the high intensity volume found in Sec. 2.4. For comparison, the first ionization volume is approximately 10^5 times larger, and the second ionization volume is approximately 10^4 times larger than the volume depicted in Fig. 2.7.

Figure 2.9 gives an example of such electron-pair trajectories in a focus. Even though the two electrons are released from the same position, they separate somewhat because of field forces since they are released at different times. Because the two electrons are released at different intensities and at potentially different laser oscillation phases, their subsequent trajectories tend to separate somewhat. Ionization at these intensities for helium can result in drift velocities of $v = 0.007 \frac{\mu m}{fs} \sin \phi$ for first ionization and $v = 0.019 \frac{\mu m}{fs} \sin \phi$ for second ionization, where ϕ represents the break-away phase (with $\phi = 0$ corresponding to the peak of the field). A reasonable range for the break-away phase turns out to be $\phi = \pm \pi/6$, which generates drift velocity ranges
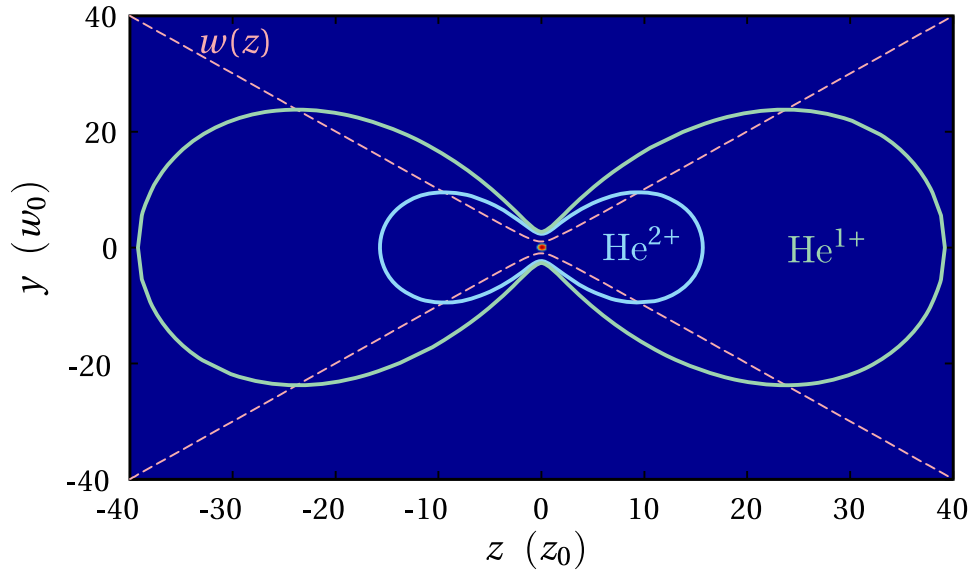
Figure 2.8 A cross section of the laser focus (side profile) showing the regions where first and second ionization of helium occurs, as well as the comparatively small high intensity region from Fig. 2.7(b) where free electrons experience the desired high intensity and their emission is redshifted. The laser parameters are $I_0 = 2 \times 10^{18}$ W/cm^2, $w_0 = 6\,\lambda_L$, $\lambda_L = 800$ nm, and $\tau_L = 35$ fs FWHM.

of $v = \pm 0.004 \frac{\mu m}{fs}$ and $v = \pm 0.010 \frac{\mu m}{fs}$ respectively along the direction of polarization. With such modest velocities, the trajectories of the electron pairs from doubly-ionized helium atoms remain correlated in the laser field over a period spanning several tens of femtoseconds. If the timescale that the electrons are free from their parent atom exceeds hundreds of femtoseconds, they tend to separate by distances greater than a wavelength.

Another relevant consideration is the quantum spreading of electrons as they interact with the laser field. Since an electron undergoes ionization over several laser cycles, a portion of the wave function bleeds away near the peak of each oscillation, but over a range of phases ϕ. This results in different portions of the same electron wave packet being released with different drift velocities, similar to the discussion in the previous paragraph where electrons from the same helium atom acquire different drift velocities. The net result is that the different electron wave functions each end up incorporating the full range of available break-away phases. The natural quantum spreading
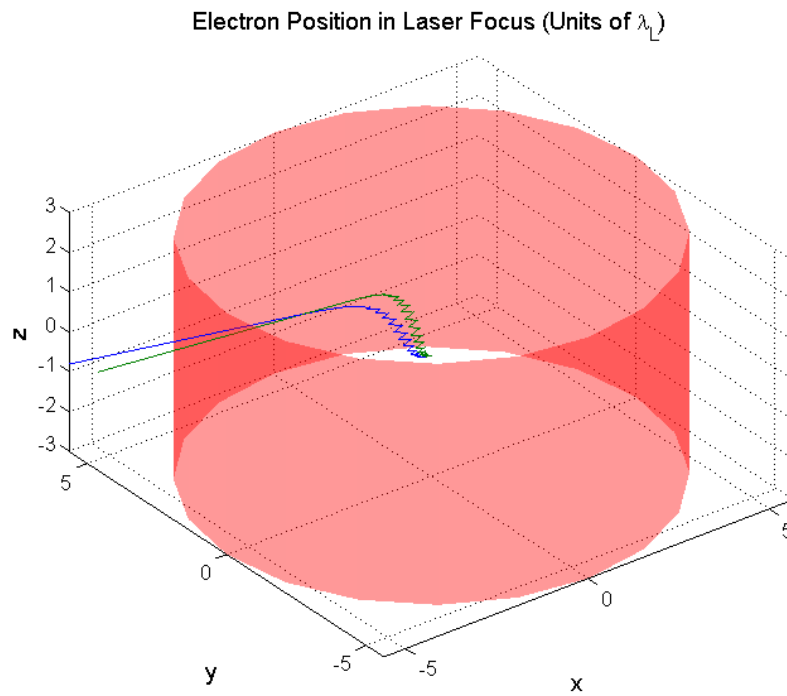
Figure 2.9 Trajectory of electrons ejected from a helium atom located at the center of the laser focus. The red outline shows the beam waist for a laser pulse with parameters $I_0 = 2 \times 10^{18}$ W/cm^2, $w_0 = 6\lambda_L$, $\lambda_L = 800$ nm, and $\tau_L = 35$ fs FWHM.

for a free electron wave packet initially the size of a helium atom occurs at a rate of $\pm 0.003 \frac{\mu m}{fs}$, which is remarkably close to the spreading due to the variety of break-away phases. Since the goal of the experiment is to measure photon scattering from large electrons, a pre-pulse arriving 100–200 fs prior to the main relativistic laser pulse may be used first to liberate the electrons from their donor atoms, and then to give the free electron wave packets time to spread to the scale of a laser wavelength.

The question of whether electron pairs from the same helium atom remain correlated during emission impacts the rate of scattered radiation by at most a factor of two. The difference in predicted signals between the first-quantized and QED viewpoints, is a range of over two orders of magnitude. Thus, the two different outcomes should be clearly distinguishable.

2.7 Radiation from the Ionization Process

In this section, we estimate the level of unwanted photoemission that might arise during the ionization of helium. In order to estimate the strength of this potential noise, the ionization process of helium was simulated using a pair of classical electrons caught in a smoothed potential well, subject to the oscillating laser field. This model has been used by Ho et al. [30] to describe nonsequential double ionization. It allows the use of an entirely classical description of the interactions between the electrons and laser field to be used. This model also allows the electrons to break free from the core naturally at the appropriate intensities for the first and second ionization of helium, and to interact with the long-range Coulomb tail of the parent ion while oscillating in the laser field. After including the softened potential interaction and computing trajectories for the electrons, we then use Eqs. (2.7)–(2.8) to estimate the electron radiation, both before and after each electron detaches from the core, while still under the influence of the Coulomb potential.

By employing this model, we find that any spectral components overlapping the redshift band-

pass region of interest arise almost entirely from the fact that the electron suddenly breaks free from the nucleus, irrespective of the specific features in the electron trajectory as it exits the atom. Essentially the same result is obtained by simply releasing an electron from rest, once the local electric field reaches the appropriate strength to cause ionization. This abrupt initiation of oscillations on the timescale of a single laser period produces faint spectral wings, independent of the model used to decide when to release the electron. This effect, though reversed in time, is similar to the spectral wings observed when computing instantaneous spectra computed when observing the interaction between an electromagnetic pulse and a linear dielectric medium [31]. Comparing the spectral wings overlapping the redshifted region of interest to the signal emitted by electrons that experience intensities of 1.5×10^{18} W/cm^2, we find that they differ by approximately three orders of magnitude. Despite this difference in signal level, because the volume undergoing ionization is enormous compared to the relevant high intensity region as shown in Fig. 2.8, it is necessary to cut out most of the ionization volume. Since the experimental setup employs a one-to-one imaging system, indeed only a small fraction of the total ionization region is actually imaged, as will be discussed in the next section.

Chapter 3

Simulating Expected Signal Levels

3.1 Redshift vs. Intensity

In order to estimate the overall signal coming from the ionization volume, the expected emission is calculated for an ensemble of free electrons given random initial positions within the double ionization region of the focus shown in Fig. 2.8. The laser parameters are the same as in Fig. 2.7 (i.e. $I_0 = 2 \times 10^{18}$ W/cm^2, $w_0 = 6\ \lambda_L$, $\lambda_L = 800$ nm, and $\tau_L = 35$ fs FWHM), which, again, are achievable pulse parameters with the current BYU setup. The resulting intensity spectra are averaged over a large number of randomly chosen individual electron trajectories, and then scaled to be representative of the total signal per laser shot depending on the density of the donor gas. For this simulation, a density associated with a helium pressure of 5×10^{-5} Torr was chosen, involving some 35,000 electrons. Effects involving possible collisions between electrons and neighboring ions are ignored. The results are shown in Fig. 3.1. They show several curves for partial volumes wherein electrons experience at least one oscillation at the various threshold intensities. Note that as the threshold intensity of the included region decreases below 1×10^{17} W/cm^2 (while keeping the peak laser intensity at 2×10^{18} w/cm^2), the signal in the spectral window of 875–925 nm does
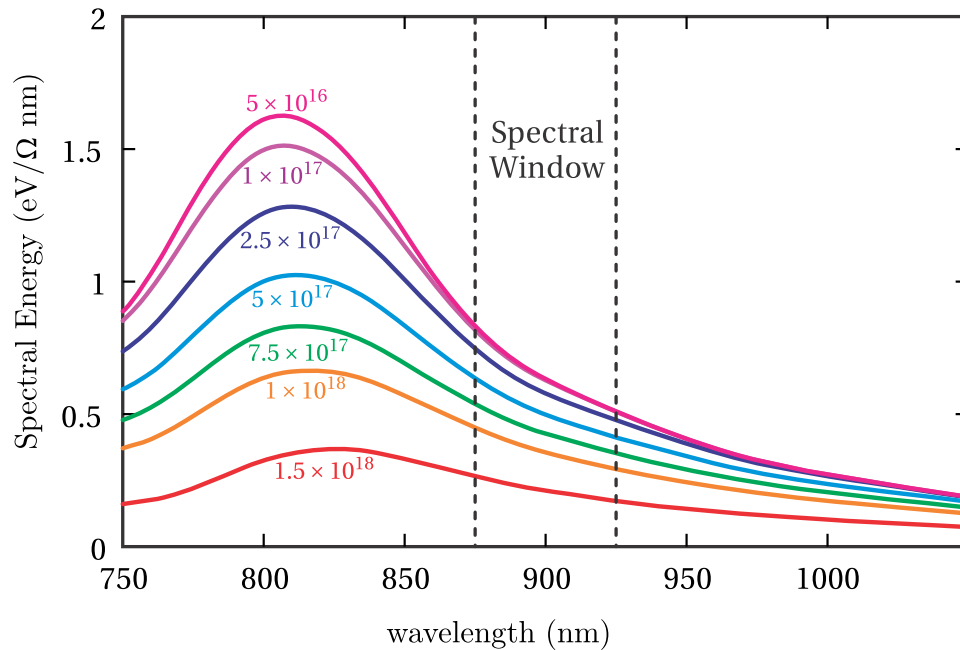
Figure 3.1 Total energy per shot for randomly distributed electrons corresponding to a pressure of 5×10^{-5} Torr. The different curves represent the radiation from the set of electrons that experience at least one laser cycle at an intensity of $15\times$, $10\times$, $7.5\times$, $5\times$, $2.5\times$, $1\times$, or 0.5×10^{17} W/cm^2. The spectrum is measured in the far field in a direction perpendicular to both the direction of laser propagation and the direction of linear laser polarization.

not significantly improve.

While the distinct spectral structure seen in Fig. 2.3 washes out in Fig. 3.1, a strong red-shift from the laser wavelength of 800 nm is clearly visible. Using the results from Fig. 3.1 and assuming a collection angle of 0.2 steradian, an 875–925 mm bandpass filter, a 5% detection efficiency, and a pressure of 5×10^{-5} Torr, a total signal for the entire ionization volume calculates to $0.7 \frac{\text{eV}}{\Omega \cdot \text{nm}} \times 50 \text{ nm} \times 0.2 \, \Omega \times 0.05 = 0.3$ eV per shot. With an average photon energy in the spectral window of about 1.4 eV, this amounts to one photon every five shots being emitted from the entire ionization volume.

3.2 Experimental Simulation

As discussed briefly in Sec. 2.7, the in-band radiation emitted from electrons during the ionization process is several orders of magnitude below the radiation emitted by the electrons exposed to the high intensities of interest. Without a method to eliminate the radiation from the majority of the much larger ionization region, the signal from the electrons of interest in the experiment would be indistinguishable from the unwanted emission from those electrons simply ionizing from their donor atoms. To remedy this problem, photons can be collected from only a section of the beam approximately one Rayleigh range z_0 in length. This size is selective enough to include the high intensity region almost completely, while cutting out the vast majority of the first and second ionization volumes. Figure 3.2 depicts this collection volume. Most of the red-shifted signal from the high intensity region is imaged into a 105 μm gold-clad multimode optical fiber as shown in Fig. 1.5. This one-to-one imaging system subtends 0.2 steradians. For comparison, the ionized volume captured by this imaging system is only 10 times larger than the relevant high intensity volume.

To simulate the overall expected signal for this experiment, helium atoms were randomly distributed throughout the imaged region of the focus at the proposed pressure of 5×10^{-5} Torr. Trajectories for the various electrons were calculated, and then used to calculate the filtered in-band signal from this distribution. This simulation was repeated and averaged to produce the results shown in Fig. 3.3. The measured energy as a function of peak laser intensity is shown, assuming a constant beam waist of $w_0 = 6 \lambda_L$, an imaging system that collects a solid angle of 0.2 steradian, and a 5% detection efficiency.

From these results, it appears that the signal becomes significant or 'turns on' at intensities between 2×10^{17} W/cm^2 and 5×10^{17} W/cm^2. At intensities below 10^{17} W/cm^2, the contribution from the ionization process in the imaged volume is apparent. At higher intensities, the primary signal is from the the redshifted electrons of interest, while the signal from other ionized electrons
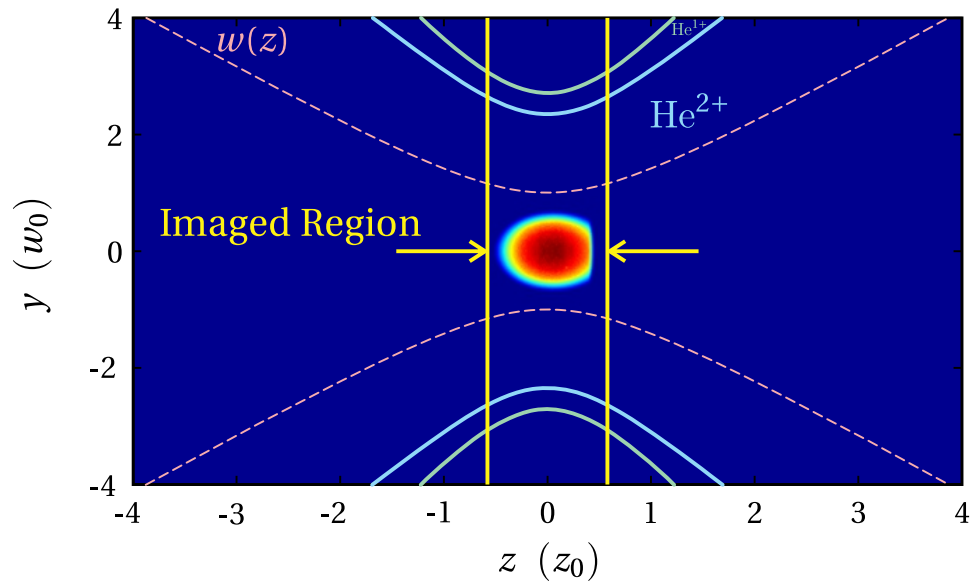
Figure 3.2 A zoomed-in portion of Fig. 2.8 showing the small portion of the focus that is imaged into the fiber. The high-intensity region from Fig. 2.7 is included for reference. As noted in Sec. 2.4, this region is asymmetrical, preferring positions before the focus, and positions offset in *y* from the laser axis rather than those offset in *x*.

Figure 3.3 Computed total energy per shot collected by the one-to-one imaging system depicted in Fig. 1.5 for varying peak intensities of a laser pulse with beam waist $w_0 = 6\lambda_L$, wavelength $\lambda_L = 800$ nm, and duration $\tau_L = 35$ fs FWHM.

contributes only about 1% of the signal. Increasing the peak laser intensity above 10^{18} W/cm^2 only gradually improves the radiated energy emitted into the target band, due in part to the tendency for the radiation to shift spatially 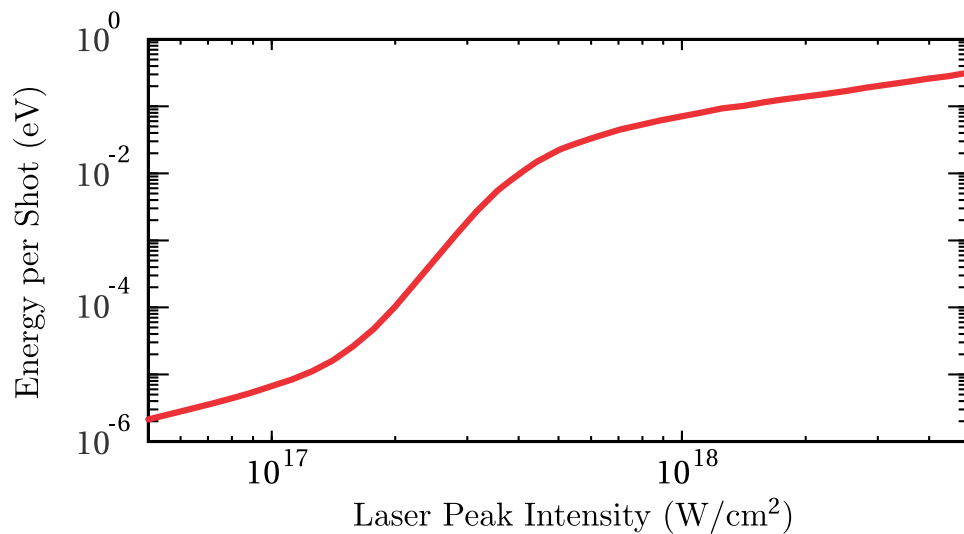towards the forward direction as the laser intensity increases. Using the proposed peak intensity of 2×10^{18} W/cm^2, the expected energy detected per shot is only 0.1 eV, or about one photon every 14 shots. This estimate is less than the one found in Sec. 3.1 because the imaging system misses a portion of the high intensity region and clips out the majority of the ionizing volume.

3.3 Conclusion and Experimental Outlook

We have simulated the classical point-charge electron trajectories in a vector representation of a focused high intensity laser pulse. These trajectories allowed the Thomson radiation scattered out the side of the laser focus to be calculated. Electrons that experience intensities near or above 1×10^{18} W/cm^2 drift in the forward direction at a significant fraction of the speed of light, causing the light scattered in the perpendicular direction to be redshifted from the laser wavelength. The proposed electron radiation experiment will measure scattered light in the vicinity of 900 nm, whereas the incident 35 fs laser pulse is centered at 800 nm. The analysis performed in this thesis suggests that the beam waist should be at least several laser wavelengths wide, perhaps $w_0 = 6 \, \lambda_L$, to enable electrons sufficient time within the focus to experience the highest intensities without being pushed out by an overly strong ponderomotive gradient.

We performed calculations to determine the effective volume of initial positions that ensures exposure to high intensity, which is significantly smaller than the actual volume enclosing that intensity. Also, this volume is significantly narrower in the dimension of laser polarization and skewed towards the upstream side of the focus. Using these results, we performed a calculation to estimate the absolute redshifted emission into the collection system of this experiment based on

a helium pressure of 5×10^{-5} Torr, which donates the free electrons as the helium atoms ionize. At this and lower pressures, the spacing between free electrons tends to be greater than half a wavelength, so the emission of the perpendicular direction sums incoherently (i.e. the intensities are added rather than the fields). Using an assumed detection efficiency of 5%, this estimate yields a photon count rate of one photon every 14 laser shots with a peak intensity near 2×10^{18} W/cm^2. This result was calculated as a function of laser intensity, and it was found that higher intensities only marginally improve the photon count rate, while intensities as low as 5×10^{17} W/cm^2 are also viable. These estimates also suggest that the emission associated with the helium ionization process redshifted into the bandpass region is sufficiently weak to ignore when only the central part of the focus is imaged into the detector.

It also seems feasible and desirable to liberate the electrons in the center of the laser focus using a pre-pulse arriving 100–200 fs prior to the main relativistic pulse to ensure that electron wave packets have the opportunity to spread to a size on par with the laser wavelength. By varying the delay of the pre-pulse, an experimental check could be performed to determine if the size of the wave packet has an impact on the emission rate. A first-quantized analysis (combined with a classical notion of the extended wave function) would suggest that the scattered emission rate is intimately connected to the size of the wave packet, with a large wave packet producing emission rates reduced by a couple orders of magnitude compared to a highly localized wave packet. On the other hand, the emission rate predicted by QED is similar in strength to classical point emitters used in the simulations performed here, regardless of the size of the actual quantum wave packet.

Bibliography

[1] Y. Salamin, S. Hu, K. Hatsagortsyan, and C. Keitel, "Relativistic high-power laser–matter interactions," Phys. Rep. **427,** 41–155 (2006).

[2] G. A. Mourou, T. Tajima, and S. V. Bulanov, "Optics in the relativistic regime," Rev. Mod. Phys. **78,** 309–371 (2006).

[3] C. I. Moore, J. P. Knauer, and D. D. Meyerhofer, "Observation of the Transition from Thomson to Compton Scattering in Multiphoton Interactions with Low-Energy Electrons," Phys. Rev. Lett. **74,** 2439–2442 (1995).

[4] S. Banerjee *et al.*, "Generation of tunable, 100–800 MeV quasi-monoenergetic electron beams from a laser-wakefield accelerator in the blowout regime," Phys. Plasmas **19,** 056703 (2012).

[5] N. D. Powers, I. Ghebregziabher, G. Golovin, C. Liu, S. Chen, S. Banerjee, J. Zhang, and D. P. Umstadter, "Quasi-monoenergetic and tunable X-rays from a laser-driven Compton light source," Nat. Photonics **8,** 28–31 (2014).

[6] X. Wang *et al.*, "Quasi-monoenergetic laser-plasma acceleration of electrons to 2 GeV," Nat. Commun. 4 (2013).

[7] W. P. Leemans, B. Nagler, A. J. Gonsalves, C. Toth, K. Nakamura, C. G. R. Geddes, E. Esarey, C. B. Schroeder, and S. M. Hooker, "GeV electron beams from a centimetre-scale accelerator," Nat Phys **2,** 696–699 (2006).

[8] E. Esarey, S. K. Ride, and P. Sprangle, "Nonlinear Thomson scattering of intense laser pulses from beams and plasmas," Phys. Rev. E **48,** 3003–3021 (1993).

[9] K. Ta Phuoc, A. Rousse, M. Pittman, J. P. Rousseau, V. Malka, S. Fritzler, D. Umstadter, and D. Hulin, "X-Ray Radiation from Nonlinear Thomson Scattering of an Intense Femtosecond Laser on Relativistic Electrons in a Helium Plasma," Phys. Rev. Lett. **91,** 195001 (2003).

[10] A. B. Murphy, "Electron Heating in the Measurement of Electron Temperature by Thomson Scattering: Are Thermal Plasmas Thermal?," Phys. Rev. Lett. **89,** 025002 (2002).

[11] J. S. Roman, L. Roso, and H. R. Reiss, "Evolution of a relativistic wavepacket describing a free electron in a very intense laser field," J. Phys. B: At. Mol. Opt. Phys. **33,** 1869 (2000).

[12] J. S. Román, L. Plaja, and L. Roso, "Relativistic quantum dynamics of a localized Dirac electron driven by an intense-laser-field pulse," Phys. Rev. A **64,** 063402 (2001).

[13] M. Mahmoudi, Y. I. Salamin, and C. H. Keitel, "Free-electron quantum signatures in intense laser fields," Phys. Rev. A **72,** 033402 (2005).

[14] A. Galkin, A. Galstyan, V. Korobkin, M. Romanovskii, and O. Shiryaev, "Charged particle motion in the field of a short laser pulse of relativistic intensity," Bulletin of the Lebedev Physics Institute **34,** 84–89 (2007).

[15] J. Peatross, C. Müller, and C. H. Keitel, "Electron wave-packet dynamics in a relativistic electromagnetic field: 3-D analytical approximation," Opt. Express **15,** 6053–6061 (2007).

[16] E. A. Chowdhury, I. Ghebregziabiher, and B. C. Walker, "Larmor radiation from the ultra-intense field ionization of atoms," J. Phys. B: At. Mol. Opt. Phys. **38,** 517 (2005).

[17] G. R. Mocken and C. H. Keitel, "Radiation spectra of laser-driven quantum relativistic electrons," Comput. Phys. Commun. **166,** 171 – 190 (2005).

[18] J. Peatross, C. Müller, K. Z. Hatsagortsyan, and C. H. Keitel, "Photoemission of a Single-Electron Wave Packet in a Strong Laser Field," Phys. Rev. Lett. **100,** 153601 (2008).

[19] J. Peatross, J. P. Corson, and G. Tarbox, "Classical connection between near-field interactions and far-field radiation and the relevance to quantum photoemission," Am J Phys **81,** 351–358 (2013).

[20] D. J. Griffiths, *Introduction to Electrodynamics*, 4th ed. (Pearson, New York, NY, 2013), pp. 449, 549.

[21] J. Corson, "Photoemission of Large Electron Wave Packets," MS Thesis (Brigham Young University, Provo, UT, 2011).

[22] J. P. Corson, J. Peatross, C. Müller, and K. Z. Hatsagortsyan, "Scattering of intense laser radiation by a single-electron wave packet," Phys. Rev. A **84,** 053831 (2011).

[23] E. Cunningham, "Photoemission by Large Electron Wave Packets Emitted out the Side of a Relativistic Laser Focus," MS Thesis (Brigham Young University, Provo, UT, 2011).

[24] F. Mackenroth, A. Di Piazza, and C. H. Keitel, "Determining the Carrier-Envelope Phase of Intense Few-Cycle Laser Pulses," Phys. Rev. Lett. **105,** 063903 (2010).

[25] E. Lötstedt and U. D. Jentschura, "Nonperturbative Treatment of Double Compton Backscattering in Intense Laser Fields," Phys. Rev. Lett. **103,** 110404 (2009).

[26] J. L. Chaloupka and D. D. Meyerhofer, "Observation of Electron Trapping in an Intense Laser Beam," Phys. Rev. Lett. **83,** 4538–4541 (1999).

[27] N. E. Rehler and J. H. Eberly, "Superradiance," Phys. Rev. A **3,** 1735–1751 (1971).

[28] S. Augst, D. Strickland, D. D. Meyerhofer, S. L. Chin, and J. H. Eberly, "Tunneling ionization of noble gases in a high-intensity laser field," Phys. Rev. Lett. **63,** 2212–2215 (1989).

[29] S. Augst, "Tunneling Ionization of Noble Gas Atoms Using a High Intensity Laser at 1 μm Wavelength," PhD Dissertation (University of Rochester, Rochester, NY, 1991).

[30] P. J. Ho, R. Panfili, S. L. Haan, and J. H. Eberly, "Nonsequential Double Ionization as a Completely Classical Photoelectric Effect," Phys. Rev. Lett. **94,** 093002 (2005).

[31] M. Ware, S. Glasgow, and J. Peatross, "Energy transport in linear dielectrics," Opt. Express **9,** 519–532 (2001).

[32] S. Bergeson and J. Peatross, "Physics 571 Lecture 5: Gaussian Beams," http://www.physics.byu.edu/faculty/bergeson/physics571/notes/L05GaussianBeams.pdf (Accessed April 18, 2012).

[33] J. D. Jackson, *Classical Electrodynamics*, 3rd ed. (Wiley, New York, 1998), pp. 461–462.

Appendix A

Laser Field Formulae

Assuming a Gaussian laser beam propagating in the $\hat{\mathbf{z}}$ direction, the expressions for the electric field components derived from a vector potential with amplitude A_0 are given by [1]

$$E_x = E\left\{S_0 + \varepsilon^2\left[\zeta^2 S_2 - \frac{\rho^4 S_3}{4}\right] + \varepsilon^4\left[\frac{S_2}{8} - \frac{\rho^2 S_3}{4} - \frac{\rho^2(\rho^2 - 16\zeta^2)S_4}{16} - \frac{\rho^4(\rho^2 + 2\zeta^2)S_5}{8} + \frac{\rho^8 S_6}{32}\right]\right\},$$

(A.1)

$$E_y = E\zeta\upsilon\left\{\varepsilon^2 S_2 + \varepsilon^4\left[\rho^2 S_4 - \frac{\rho^4 S_5}{4}\right]\right\},$$

(A.2)

$$E_z = E\zeta\left\{\varepsilon C_1 + \varepsilon^3\left[-\frac{C_2}{2} + \rho^2 C_3 - \frac{\rho^4 C_4}{4}\right] + \varepsilon^5\left[-\frac{3C_3}{8} - \frac{3\rho^2 C_4}{8} + \frac{17\rho^4 C_5}{16} - \frac{3\rho^6 C_6}{8} + \frac{\rho^8 C_7}{32}\right]\right\}.$$

(A.3)

The magnetic field components are then given by

$$B_x = 0,$$

(A.4)

$$B_y = E\left\{S_0 + \varepsilon^2\left[\frac{\rho^2 S_2}{2} - \frac{\rho^4 S_3}{4}\right] + \varepsilon^4\left[\frac{-S_2}{8} + \frac{\rho^2 S_3}{4} + \frac{5\rho^4 S_4}{16} - \frac{\rho^6 S_5}{4} + \frac{\rho^8 S_6}{32}\right]\right\},$$

(A.5)

$$B_z = E\upsilon\left\{\varepsilon C_1 + \varepsilon^3\left[\frac{C_2}{2} + \frac{\rho^2 C_3}{2} - \frac{\rho^4 C_4}{4}\right] + \varepsilon^5\left[\frac{3C_3}{8} + \frac{3\rho^2 C_4}{8} + \frac{3\rho^4 C_5}{16} - \frac{\rho^6 C_6}{4} + \frac{\rho^8 C_7}{32}\right]\right\}.$$

(A.6)

Furthermore, the parameter $\varepsilon = w_0/z_r$ is the diffraction angle with w_0 the beam waist at the focus and z_r the Rayleigh range. The parameters $\zeta = x/w_0$ and $\upsilon = y/w_0$ are reduced lengths. Also, letting $w(z) = w_0\sqrt{1 + (z/z_r)^2}$ we make the remaining definitions in the field expressions

$$E = E_0 \frac{w_0}{w} exp\left[-\frac{r^2}{w^2}\right]; \quad E_0 = kA_0, \tag{A.7}$$

$$S_n = \left(\frac{w_0}{w}\right)^n sin(\psi + n\psi_G), \tag{A.8}$$

$$C_n = \left(\frac{w_0}{w}\right)^n cos(\psi + n\psi_G) \tag{A.9}$$

where $k = \omega/c$, $\rho = r/w_0$, and $\psi = \psi_0 + \psi_P - \psi_R + \psi_G$. Finally, we define ψ_0 to be the constant phase, $\psi_P = \omega t - kz$ the plane wave phase, $\psi_R = kr^2/(2R)$ with $R(z) = z + z_r^2/z$ the phase associated with the curvature of the wave fronts, and $\psi_G = tan^{-1}(z/z_r)$ the Guoy phase.

Appendix B

Over Barrier Ionization

In an intense laser field, the potential that an electron feels is a combination of the Coulomb and laser field which may be written in one-dimension as

$$V(x,t) = -\frac{ne^2}{4\pi\varepsilon_0|x|} - eE_0 x\cos(\omega_L t),\tag{B.1}$$

where n is the charge state of the ion left behind. An estimate for the laser field necessary for ionization can be obtained by calculating the field strength needed to suppress the Coulomb barrier until its peak is the same as the binding energy of the atom or ion [28].

The peak field occurs when $\cos(\omega_L t) = \pm 1$. The location of the top of the barrier may be found from

$$\left.\frac{dV}{dx}\right|_{x>0} = \frac{ne^2}{4\pi\varepsilon_0 x_{\text{peak}}^2} - eE_0 = 0 \Rightarrow x_{\text{peak}} = \sqrt{\frac{ne}{4\pi\varepsilon_0 E_0}}.\tag{B.2}$$

This location can then be substituted into Eq. (B.1) to determine the value of the potential at the peak which gives

$$V(x_{\text{peak}}) = -\sqrt{\frac{ne^3 E_0}{\pi\varepsilon_0}}.\tag{B.3}$$

Setting this value equal to the binding energy, we can determine the electric field necessary for

ionization to occur and subsequently the required intensity:

$$\Phi = -\sqrt{\frac{ne^3 E_0}{\pi \varepsilon_0}} \Rightarrow E_0 = \frac{\pi \varepsilon_0}{ne^3} \Phi^2 \Rightarrow I_\Phi = \frac{1}{2} \varepsilon_0 c E_0^2 = \frac{\pi^2 c \varepsilon_0^3}{2e^6} \frac{\Phi^4}{n^2}. \tag{B.4}$$

The ionization potential for the first and second electrons in helium are 24 and 54.4 eV, respectively. Using the formula given in Eq. (B.4), the ionization intensities are thus 1.3×10^{15} and 8.7×10^{15} W/cm^2, respectively.

Next, we compute the volume enclosed by an intensity threshold I_Φ within a laser focus. The intensity distribution in the laser focus is given by [32]

$$I = \frac{I_0}{1 + z^2/z_0^2} \exp\left[-\frac{2\rho^2}{w_0^2(1 + z^2/z_0^2)}\right]. \tag{B.5}$$

We are interested in the volume wherein the intensity exceeds the ionization intensity Eq. (B.4). The differential volume element is defined as $dV = \pi \rho^2 dz$, so setting the intensity in Eq. (B.5) equal to the threshold intensity in Eq. (B.4), we can invert the equation and define

$$\rho^2 = -\frac{w_0^2(1 + z^2/z_0^2)}{2} \ln\left[\frac{I_\Phi}{I_0}(1 + z^2/z_0^2)\right], dV = -\frac{\pi w_0^2(1 + z^2/z_0^2)}{2} \ln\left[\frac{I_\Phi}{I_0}(1 + z^2/z_0^2)\right] dz. \tag{B.6}$$

Integrating over z, we then obtain an expression for the volume as a function of intensity given by

$$V(I_0, I_\Phi) = \frac{2\pi w_0^2 z_0}{3} \left[\frac{1}{3}\left[\frac{I_0}{I_\Phi} - 1\right]^{3/2} + 2\sqrt{\frac{I_0}{I_\Phi} - 1} - 2\tan^{-1}\left(\sqrt{\frac{I_0}{I_\Phi} - 1}\right)\right]. \tag{B.7}$$

This expression gives the volume inside the laser focus wherein the intensity exceeds the ionization threshold. This is important for determining the number of helium atoms that become ionized in our experiment. To estimate this value, I use some reasonable experimental parameters where $w_0 = 6\,\lambda_L$, $I_0 = 2 \times 10^{18}$W/cm^3, and the pressure is 10^{-5} Torr. With these values, approximately 9 helium atoms will be found in the region of highest intensity where $I > 1.5 \times 10^{18}$ W/cm^2, whereas approximately 1×10^6 atoms are found within the region where $I > 1.3 \times 10^{15}$ W/cm^2. Figure B.1 shows the regions within such a focus where first and second ionization of helium occurs, as well as the comparatively small region where $I > 1.5 \times 10^{18}$ W/cm^2.
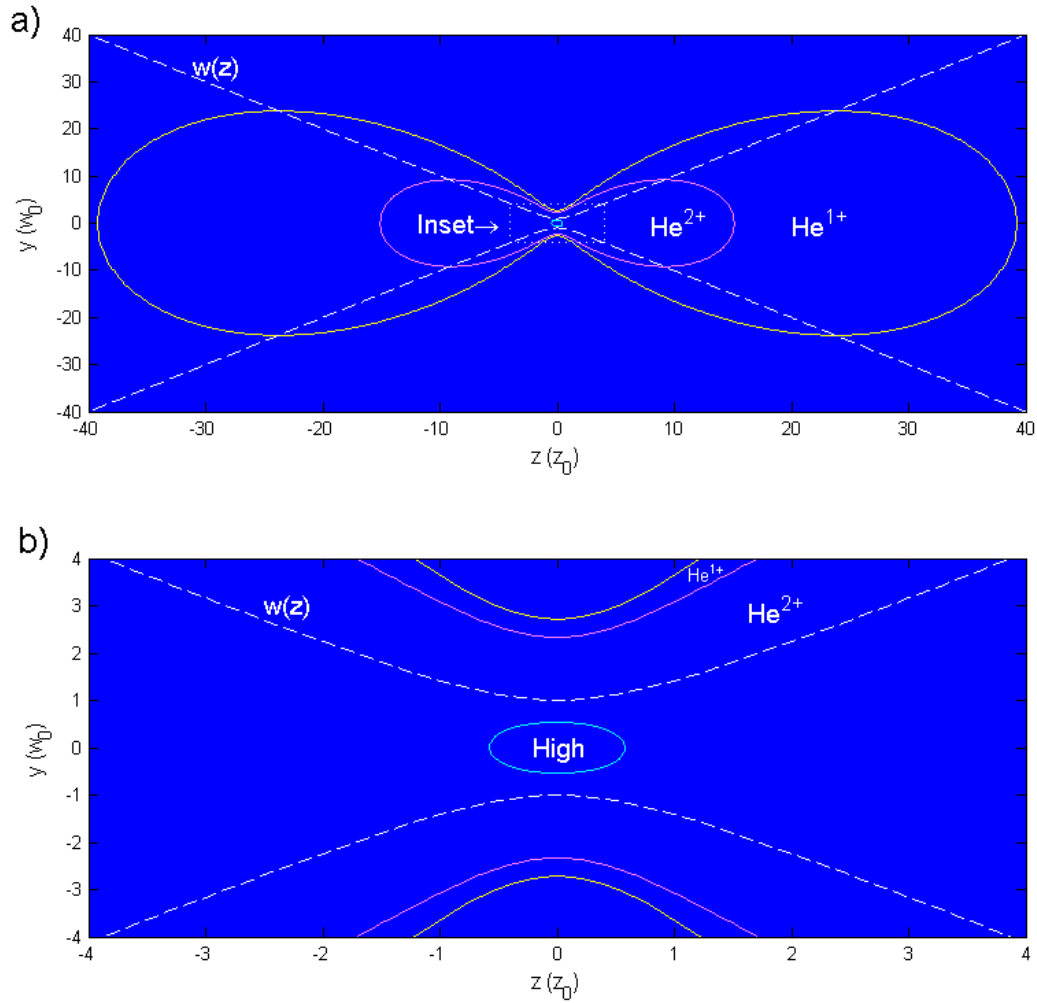
Figure B.1 A cross section of the laser focus (side profile) showing the regions where first and second ionization of helium occurs, as well as the comparatively small high intensity region where $I > 1.5 \times 10^{18}$ W/cm^2. The image in a) shows an overview of the entire focus while the image in b) is an expanded view of the central part of the focus to show the much smaller high intensity region. The laser parameters are $I_0 = 2 \times 10^{18}$ W/cm^2, $w_0 = 6 \, \lambda_L$, $\lambda_L = 800$ nm, and $\tau_L = 35$ fs FWHM.

Appendix C

Comparison of Emission from a Single Atom and a Collection of Atoms

It is illustrative to demonstrate some important results comparing emission from a single atom to that of an ensemble of atoms. To begin, the distinction between continuous media and an ensemble of randomly distributed discrete emitters is made, the latter being similar to the gas target in the electron radiation experiment. We contrast a fluid-like electric current model with a Gaussian spatial distribution to a similar distribution of discrete dipole emitters.

C.1 Emission from a Continuous Distribution

Consider a classical current distribution describing a continuous medium that oscillates with the form [19]:

$$\mathbf{J}\left(\mathbf{r}',t\right) = \hat{z}J_0 e^{-\left(\frac{x'^2}{x_0^2} + \frac{y'^2}{y_0^2} + \frac{z'^2}{z_0^2}\right)} \sin\left(kx' - \omega t\right). \tag{C.1}$$
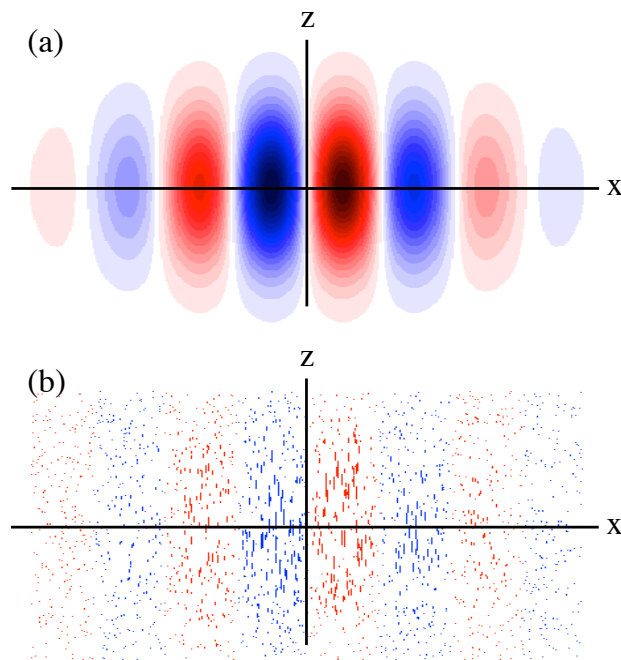
47

Figure C.1 (a) *x-z* slice of a current distribution defined by Eq. (C.1), at a given instant in time. The direction of the current alternates with each segment (color coded) and is polarized in the *z*-direction. The internal waves propagate in the *x*-direction at speed *c* while the overall Gaussian distribution remains centered on the origin. (b) Randomly positioned dipoles whose strengths and phases are similar to the pattern in (a). Each dipole is represented by a line proportional to its instantaneous strength.

This current distribution is depicted in Fig. C.1(a). Such a distribution might be analogous to a polarizeable medium stimulated by an electric field propagating in the *x*-direction, such as a laser field, polarized in the *z*-direction with frequency $\omega = ck$. Such a Gaussian profile roughly approximates the region within a laser focus where atoms might respond nonlinearly to the intensity.

The electric field in the far-field limit would then be given by [19]

$$\mathbf{E}\left(\mathbf{r},t\right) = \frac{1}{4\pi\varepsilon_0 c^2} \int^{t_r} \frac{d^3 r'}{r_{ret}} \left[\left(\dot{\mathbf{J}}\left(\mathbf{r}',t_r\right)\cdot\hat{\mathbf{r}}_{ret}\right)\hat{\mathbf{r}}_{ret} - \dot{\mathbf{J}}\left(\mathbf{r},t_r\right)\right] \tag{C.2}$$

with $\mathbf{r}_{ret} \equiv \mathbf{r} - \mathbf{r}'$ and $t_r \equiv t - r_{ret}/c$ [19]. In the far-field limit, we may also use the simplifications $\hat{\mathbf{r}}_{ret} \equiv \mathbf{r}_{ret}/r_{ret} \cong \hat{r}$ and $r_{ret} \cong r - \mathbf{r}'\cdot\hat{r}$, with $r_{ret} \cong r$ in the denominator. With Eq. (1.1) substituted into Eq. (C.2) the result becomes

$$\mathbf{E}\left(\mathbf{r},t\right) \cong -\frac{kJ_0}{4\pi\varepsilon_0 cr}\left(\left(\hat{z}\cdot\hat{r}\right)\hat{r} - \hat{z}\right) \int e^{-\left(\frac{x'^2}{x_0^2} + \frac{y'^2}{y_0^2} + \frac{z'^2}{z_0^2}\right)} \cos\left(kx' - \omega t + kr - k\frac{x'x + y'y + z'z}{r}\right) dx' dy' dz'. \tag{C.3}$$

This Gaussian integration can be performed analytically, then time-averaged to obtain the time-averaged Poynting vector directed along $\hat{r}$ given by

$$I \equiv \langle S\rangle_t = \varepsilon_0 c\left\langle \mathbf{E}^2\right\rangle_t = \frac{\varepsilon_0 c k^4 \sin^2\theta}{2\left(4\pi\varepsilon_0\right)^2 r^2}\left(\frac{J_0}{\omega}\pi^{3/2}x_0 y_0 z_0\right)^2 e^{-\frac{k^2}{2}\left(x_0^2\left(1-\frac{x}{r}\right)^2 + y_0^2\frac{y^2}{r^2} + z_0^2\frac{z^2}{r^2}\right)} \tag{C.4}$$

with θ being the angle $\hat{r}$ makes with the *z* axis. The far-field emission pattern for three different distribution sizes is shown in Fig. C.2. For small distributions, such as when $kx_0 \ll 1, ky_0 \ll 1$, the emission is fairly uniform throughout the $x-y$-plane and resembles the pattern of a single dipole emitter. However, as the size of the current distribution grows, interference from different parts causes radiation emitted in directions perpendicular to the propagating electric field to be suppressed. In the forward, or propagation direction, the irradiance remains a constant factor proportional to $(x_0 y_0 z_0 J_0)^2$. Such constructive interference in the direction of propagation is the well known phenomenon of phase matching.

As indicated in Fig. C.2, as the distribution grows in size, emission in directions other than $\hat{x}$ falls dramatically. This is a well known characteristic of continuous distributions as well as ordered
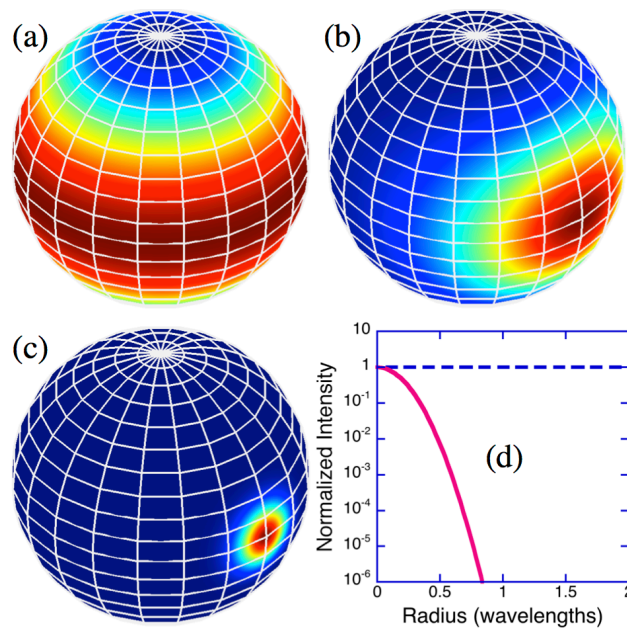
Figure C.2 Far-field average Poynting flux from a Gaussian current distribution according to Eq. (C.4) with distribution sizes (a) $r_0 = 0$, (b) $r_0 = \lambda/4$, (c) $r_0 = \lambda$, with $r_0 = \sqrt{x_0^2 + y_0^2 + z_0^2}$ and $x_0 = y_0 = z_0$. (d) shows the exponential factor in Eq. (C.4) for the forward (dashed) and perpendicular (solid) emission directions.

arrays of discrete emitters, with cancellation into poorly phase-matched directions becoming significant as the distribution becomes only a few wavelengths across. Next, this analysis is extended to a collection of randomly distributed dipoles.

C.2   Emission From an Ensemble of Dipoles

To begin the analysis, the expression for a single dipole oriented along $\hat{z}$, positioned at $\mathbf{r}_n$, oscillating with frequency $\omega = ck$ is given by

$$\mathbf{p}_n = \hat{z} p_{0n} \cos\left(-\omega t + \varphi_n\right). \tag{C.5}$$

where p_{0n} and φ_n represent the amplitude and phase, respectively. Such a dipole could represent a particular oscillating frequency component of an atom located at $\mathbf{r}_n$, a particular harmonic of the driving laser field, for example.

In the far field, the electric field such a dipole radiates may be written as

$$\mathbf{E}_n\left(\mathbf{r},t\right) \cong -\hat{\theta}\sin\theta \frac{k^2}{4\pi\varepsilon_0 r}p_{0n}\cos(kr_{ret} - \omega t + \varphi_n) \tag{C.6}$$

with $\mathbf{r}_{ret} \equiv \mathbf{r} - \mathbf{r}_n$ and $r_{ret} \cong r - \mathbf{r}_n \cdot \hat{r}$ [33]. For comparison with the Gaussian current distribution used previously, the strength of each individual dipole is chosen to be $p_{0n} = p_0 e^{-(x_n^2/x_0^2 + y_n^2/y_0^2 + z_n^2/z_0^2)}$, and the phase to be $\varphi_n = kx_n$. Next, the electric fields are summed for collection of dipoles distributed randomly throughout space, analogous to a collection of atoms in a gas backfilled into a vacuum chamber wherein a laser is focused, for example.

The time-averaged Poynting flux from such a distribution of dipoles can be written as

$$I \equiv \langle S\rangle_t = c\varepsilon_0 \left\langle \left[\sum_n \mathbf{E}_n\right]^2 \right\rangle_t = \frac{c\varepsilon_0 k^4 \sin^2\theta}{2\left(4\pi\varepsilon_0\right)^2 r^2}p_0^2 \left|\sum_n e^{-\left(\frac{x_n^2}{x_0^2} + \frac{y_n^2}{y_0^2} + \frac{z_n^2}{z_0^2}\right)} e^{-ik\left(x_n\left(1 - \frac{x}{r}\right) - y_n\frac{y}{r} - z_n\frac{z}{r}\right)}\right|^2 . \tag{C.7}$$

The portion of this expression in with the absolute-value squared is called the "structure factor" [33], and generally may not have an analytical expression, so it must be computed numerically. Note, however, that this expression agrees with Eq. (C.4) for directions that are well

phase-matched. In particular, if the observation point is $\mathbf{r} = x\hat{x}$, the complex exponential in Eq. (C.7) collapses to unity, so the expectation of the structure factor can be written as

$$p_0^2 \left| \sum_n e^{-\left(\frac{x_n^2}{x_0^2} + \frac{y_n^2}{y_0^2} + \frac{z_n^2}{z_0^2}\right)} \right|^2 \rightarrow p_0^2 \left[n_V \int e^{-\left(\frac{x_n^2}{x_0^2} + \frac{y_n^2}{y_0^2} + \frac{z_n^2}{z_0^2}\right)} dx_n dy_n dz_n \right]^2 = \left(p_0 n_V \pi^{3/2} x_0 y_0 z_0 \right)^2 \equiv p_{\text{eff}}^2 N_{\text{eff}}^2 \tag{C.8}$$

where n_V is the density of dipoles. In Eq. (C.4), J_0/ω also has units of dipoles per unit volume, and serves the role $p_0 n_V$ does in this expression. Thus, in the limit where there is a large number of participating dipoles, and in the direction of good phase-matching, Eqs. (C.4) and (C.7) provide identical results. For convenience in the subsequent analysis, an effective dipole amplitude is defined as $p_{eff} \equiv p_0/2^{3/2}$ and an effective number of participating dipoles as $N_{eff} \equiv n_V (2\pi)^{3/2} x_0 y_0 z_0$.

Now, in contrast with the coherent result derived above, in poorly phase matched directions (i.e. when $kx_0(1 - x/r) \gtrsim \pi$, $ky_0 y/r \gtrsim \pi$, or $kz_0 z/r \gtrsim \pi$), the randomized locations (x_n, y_n, z_n) causes the expectation of the structure factor to reduce to the well established incoherent result

$$p_0^2 \sum_n e^{-2\left(\frac{x_n^2}{x_0^2} + \frac{y_n^2}{y_0^2} + \frac{z_n^2}{z_0^2}\right)} \rightarrow p_0^2 n_V \int e^{-2\left(\frac{x_n^2}{x_0^2} + \frac{y_n^2}{y_0^2} + \frac{z_n^2}{z_0^2}\right)} dx_n dy_n dz_n = p_{\text{eff}}^2 N_{\text{eff}} \tag{C.9}$$

when the number of dipoles grows sufficiently large. In this case, the emission is reduced by a factor of N_{eff}. These results, depicted in Fig. C.3 for a randomly distributed collection of coherent dipoles, agrees with the Gaussian fluid model in directions where phase-matching exceeds $1/N_{eff}$ times the peak value. Inclusion of the Guoy shift or other phase mismatches would only impact emission in phase-matched directions.

Now, if φ_n were randomly assigned, then Eq. (C.9) would apply to any observation direction, eliminating any phase-matching, as shown in Fig. C.3. The results in Fig. C.3 were generated numerically using Eq. (C.7). Notice that in poorly phase-matched directions, emission strength is the same regardless of whether the dipoles are emitting coherently or incoherently. In other words, the randomness of the dipole locations, so long as the distribution size exceeds wavelength, produces the same result as if the emission phase were inherently random.
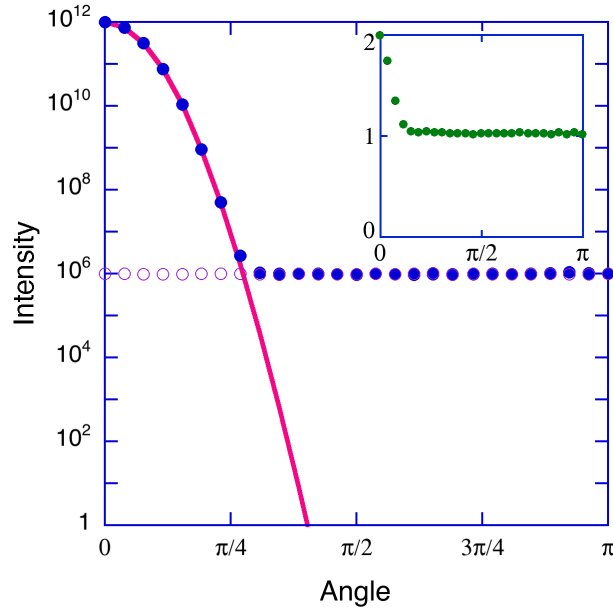
Figure C.3 Emission as a function of angle $\phi = \tan^{-1}\left(\frac{y}{x}\right)$ with $x_0, y_0, z_0 = \lambda$ for a continuous distribution according to Eq. (C.4) (line), a distribution of randomly located coherent dipoles according to Eq. (C.7) (filled circles), and a similar distribution dipoles that emit with a randomly selected phase $\pm\pi$ (open circles). N_{eff} was chosen to be 10^6, and each point represents the average of 1000 trials involving randomly selected full ensembles. The inset shows the intensity for the case of $N_{\text{eff}} = 1$ plotted on a linear scale (averages of 50,000 trials).

C.3 Conclusions

In the previous examples of a Gaussian distribution and a collection of dipole emitters, there are a few important observations to make. First, the volume being excited need only exceed one wavelength to obtain characteristically incoherent emission into poorly phase-matched directions. Second, that this property remains true even when there is effectively only a single emitter within the focal volume. These properties are particularly important for interpreting the results in the electron-scattering experiment, where the densities of atoms should be fairly low.

Index